

GENERATIVE ENTROPIC NEURAL OPTIMAL TRANSPORT TO MAP WITHIN AND ACROSS SPACES

Dominik Klein^{*,†,1} Théo Uscidda^{*,2} Fabian J. Theis¹ Marco Cuturi³

¹Helmholtz Munich & TU Munich ²CREST-ENSAE ³Apple

ABSTRACT

Learning measure-to-measure mappings is a crucial task in machine learning, featured prominently in generative modeling. Recent years have witnessed a surge of techniques that draw inspiration from optimal transport (OT) theory. Combined with neural network models, these methods collectively known as *Neural OT* use optimal transport as an inductive bias: such mappings should be optimal w.r.t. a given cost function, in the sense that they are able to move points in a thrifty way, within (by minimizing displacements) or across spaces (by being isometric). This principle, while intuitive, is often confronted with several practical challenges that require adapting the OT toolbox: cost functions other than the squared-Euclidean cost can be challenging to handle, the deterministic formulation of Monge maps leaves little flexibility, mapping across incomparable spaces raises multiple challenges, while the mass conservation constraint inherent to OT can provide too much credit to outliers. While each of these mismatches between practice and theory has been addressed independently in various works, we propose in this work an elegant framework to unify them, called *generative entropic neural optimal transport* (GENOT). GENOT can accommodate any cost function; handles randomness using conditional generative models; can map points across incomparable spaces, and can be used as an *unbalanced* solver. We evaluate our approach through experiments conducted on various synthetic datasets and demonstrate its practicality in single-cell biology. In this domain, GENOT proves to be valuable for tasks such as modeling cell development, predicting cellular responses to drugs, and translating between different data modalities of cells.

1 INTRODUCTION

Mapping a probability distribution onto another is a ubiquitous challenge in machine learning, with many implications in the field of generative modeling. Optimal transport (OT) has arisen in a few years as a major purveyor of tools to better address these challenges, both in theory and practice. The focus of OT lies on finding maps that can effectively transform a distribution of matter onto another, by minimizing a certain notion of cost (Santambrogio, 2015). Originally rooted in physics, the application of OT to large-dimensional problems arising in machine learning and sciences has necessitated various modifications and adaptations. Starting with solvers that can solve approximate matching problems at large scales (Cuturi, 2013; Peyré et al., 2016; Scetbon et al., 2021; 2022), a recent plethora of OT-inspired training approaches for neural networks has emerged (Makkuva et al., 2020; Korotin et al., 2020; Asadulaev et al., 2022; Fan et al., 2020; Uscidda & Cuturi, 2023; Lipman et al., 2023; Tong et al., 2020; 2023b). As an illustration of this overall trend, the applications of OT to single-cell genomics have evolved from advanced matching problems (Schiebinger et al., 2019; Demetci et al., 2022), towards neural-based approaches that can, for instance, predict the response of cells to various perturbations (Bunne et al., 2021; 2022). Our goal in this paper is to address the various challenges that still stand in the way of applying OT to the most pressing scientific tasks.

From Linear to Quadratic Neural OT Maps. Optimal transport is primarily used through the Kantorovich problem to put in correspondence distributions taking values in the same space \mathcal{X} , pending the existence of a cost $c(x, y)$ for any two points $x, y \in \mathcal{X}$. Most of the theory is available

^{*}Equal contribution

[†]Work done during an internship at Apple

in that regime, notably for simpler costs such as the squared Euclidean distance (Santambrogio, 2015, §1.3). We refer to such problems as *linear* OT problems. Yet, more challenging applicative scenarios sought by practitioners involve source and target distributions that do *not* live in the same space, e.g. \mathcal{X} and \mathcal{Y} have differing dimensions, as in (Demetci et al., 2022). The challenge in that case is that no cost functions are known, requiring the use of quadratic losses (Mémoli, 2011; Sturm, 2020), yielding the so-called Gromov-Wasserstein (GW) problem. While theory is far more scarce in these regimes, practitioners expressed major interest in that flexibility, going as far as proposing, with the Fused Gromov-Wasserstein (FGW) distance, a tool that blends both linear and quadratic approaches (Vayer et al., 2018), as in (Klein et al., 2023; Lange et al., 2023; Nitzan et al., 2019; Zeira et al., 2022). There exists, however, to our knowledge, only one formulation of a neural quadratic OT method, which is limited to learning deterministic maps for the inner product costs and whose training procedure involves a min-max-min optimization procedure (Nekrashevich et al., 2023).

From Deterministic to Stochastic Maps. The classic (Monge) deterministic map can lack flexibility in practice, both at estimation and inference time. In the quadratic case, that map may not exist (Dumont et al., 2022). Practitioners may favor, instead, stochasticity, which would account naturally for instance, for the non-determinism of cell evolutions (Elowitz et al., 2002). Stochastic formulations can also produce a conditional distribution that can be used to quantify uncertainty. In the discrete setting, this property is fulfilled by entropy-regularized OT (EOT) (Cuturi, 2013).

Flexibility in Mass Conservation. In numerous real-world applications, the data acquisition process can be error-prone, resulting in outliers. To mitigate this, unbalanced OT (UOT) formulations that can discard observations have been proposed (Frogner et al., 2015; Chizat et al., 2018; Séjourné et al., 2021), with numerous applications to generative modeling (Balaji et al., 2020; Yang & Uhler, 2019) and single-cell genomics (Schiebinger et al., 2019; Eyring et al., 2022; Lübeck et al., 2022).

Contributions. We propose a flexible neural OT framework that satisfies all requirements above:

- We propose the first method to compute neural EOT couplings in both Kantorovich and GW settings by fitting stochastic maps to their conditional distributions (Prop. 3.1) using conditional flow matching (Lipman et al., 2023) as a building block. In particular, GENOT works with any cost function between samples.
- By showing that solving an unbalanced EOT problem is equivalent to solving a balanced one between re-weighted measures (Prop. 3.2) that can be estimated consistently (Prop. 3.3), we introduce U-GENOT to solve unbalanced EOT problems.
- We extend (U-)GENOT to solve the (unbalanced) entropic Fused GW problem (§ 3.3). To our knowledge, GENOT is the first neural OT method to solve a continuous Fused GW problem.
- We demonstrate the applicability of GENOT in various single-cell biology problems. In particular, we (i) quantify lineage branching events in the developing mouse pancreas, (ii) predict cellular responses to drug perturbations along with a well-calibrated uncertainty estimation, and (iii) introduce a novel method to translate ATAC-seq data to RNA-seq data.

2 BACKGROUND

Notations. We consider throughout this work two compact subsets $\mathcal{X} \subset \mathbb{R}^p$, $\mathcal{Y} \subset \mathbb{R}^q$, referred to as the source and the target domain, respectively. In general, $p \neq q$. The sets of positive measures and probability measures on \mathcal{X} are denoted by $\mathcal{M}^+(\mathcal{X})$ and $\mathcal{M}_1^+(\mathcal{X})$, respectively. For $\pi \in \mathcal{M}^+(\mathcal{X} \times \mathcal{Y})$, we denote its marginals by $\pi_1 := p_1 \# \pi$ and $\pi_2 := p_2 \# \pi$. Then, for $\mu \in \mathcal{M}^+(\mathcal{X})$, $\nu \in \mathcal{M}^+(\mathcal{Y})$, $\Pi(\mu, \nu)$ is the set of probability measures with respective marginals μ and ν , i.e. $\Pi(\mu, \nu) = \{\pi : \pi_1 = \mu, \pi_2 = \nu\} \subset \mathcal{P}(\mathcal{X} \times \mathcal{Y})$. We define $\frac{d\mu}{d\nu}$ to be the relative density of μ w.r.t. ν and write $\mu = \frac{d\mu}{d\nu} \cdot \nu$ accordingly. For $\rho, \gamma \in \mathcal{M}^+(\mathcal{X})$, $\text{KL}(\rho|\gamma) = \int_{\mathcal{X}} \log(\frac{d\rho}{d\gamma}) d\rho - \int_{\mathcal{X}} d\gamma + \int_{\mathcal{X}} d\rho$.

2.1 ENTROPIC OPTIMAL TRANSPORT

The Entropic Kantorovich Problem. Let $c : \mathcal{X} \times \mathcal{Y} \rightarrow \mathbb{R}$ be a cost function, $\mu \in \mathcal{M}_1^+(\mathcal{X})$, $\nu \in \mathcal{M}_1^+(\mathcal{Y})$ and $\varepsilon \geq 0$. The entropy-regularized OT problem reads

$$\min_{\pi \in \Pi(\mu, \nu)} \int_{\mathcal{X} \times \mathcal{Y}} c(\mathbf{x}, \mathbf{y}) d\pi(\mathbf{x}, \mathbf{y}) + \varepsilon \text{KL}(\pi | \mu \otimes \nu). \quad \text{EK}$$

A solution π_ε^* of (EK) always exists. With $\varepsilon = 0$, we recover the classical Kantorovich (1942) problem. When $\varepsilon > 0$, the optimal coupling π_ε^* is unique. If μ and ν are discrete, (EK) can be solved with the Sinkhorn algorithm (Cuturi, 2013).

The Entropic Gromov-Wasserstein Problem. As opposed to considering an *inter-domain* cost defined on $\mathcal{X} \times \mathcal{Y}$, the entropic Gromov-Wasserstein problem is concerned with seeking couplings based on *intra-domain* cost functions $c_{\mathcal{X}} : \mathcal{X} \times \mathcal{X} \rightarrow \mathbb{R}$ and $c_{\mathcal{Y}} : \mathcal{Y} \times \mathcal{Y} \rightarrow \mathbb{R}$:

$$\min_{\pi \in \Pi(\mu, \nu)} \int_{(\mathcal{X} \times \mathcal{Y})^2} |c_{\mathcal{X}}(\mathbf{x}, \mathbf{x}') - c_{\mathcal{Y}}(\mathbf{y}, \mathbf{y}')|^2 d\pi(\mathbf{x}, \mathbf{y}) d\pi(\mathbf{x}', \mathbf{y}') + \varepsilon \text{KL}(\pi | \mu \otimes \nu). \quad \text{EGW}$$

With $\varepsilon = 0$, we recover the Gromov-Wasserstein problem (Mémoli, 2011). As in the Kantorovich setting, using $\varepsilon > 0$ comes with favorable computational properties, since for discrete μ, ν , we can solve (EGW) with a mirror-descent scheme based on the Sinkhorn algorithm (Peyré et al., 2016).

Unbalanced Extensions. The EOT formulations presented above can only handle measures with the same total mass. Unbalanced optimal transport (UOT) (Liero et al., 2018; Chizat et al., 2018) lifts this constraint by penalizing the deviation of $p_1 \# \pi$ to μ and $p_2 \# \pi$ to ν with a divergence. Using the KL divergence and introducing $\lambda_1, \lambda_2 > 0$ controlling how much mass variations are penalized as opposed to transportation, the unbalanced extension of (EK) seeks a measure $\pi \in \mathcal{M}^+(\mathcal{X} \times \mathcal{Y})$:

$$\min_{\pi \in \mathcal{M}^+(\mathcal{X} \times \mathcal{Y})} \int_{\mathcal{X} \times \mathcal{Y}} c(\mathbf{x}, \mathbf{y}) d\pi(\mathbf{x}, \mathbf{y}) + \varepsilon \text{KL}(\pi | \mu \otimes \nu) + \lambda_1 \text{KL}(\pi_1 | \mu) + \lambda_2 \text{KL}(\pi_2 | \nu). \quad \text{UEK}$$

This problem can be solved efficiently in a discrete setting using a variant of the Sinkhorn algorithm (Frogner et al., 2015; Séjourné et al., 2023a). Analogously, the GW formulation (EGW) also admits an unbalanced generalization, which reads

$$\begin{aligned} \min_{\pi \in \mathcal{M}^+(\mathcal{X} \times \mathcal{Y})} \int_{(\mathcal{X} \times \mathcal{Y})^2} |c_{\mathcal{X}}(\mathbf{x}, \mathbf{x}') - c_{\mathcal{Y}}(\mathbf{y}, \mathbf{y}')|^2 d\pi(\mathbf{x}, \mathbf{y}) d\pi(\mathbf{x}', \mathbf{y}') \\ + \varepsilon \text{KL}^\otimes(\pi | \mu \otimes \nu) + \lambda_1 \text{KL}^\otimes(\pi_1 | \mu) + \lambda_2 \text{KL}^\otimes(\pi_2 | \nu), \end{aligned} \quad \text{UEGW}$$

where $\text{KL}^\otimes(\rho | \gamma) = \text{KL}(\rho \otimes \rho | \gamma \otimes \gamma)$. This can also be solved using an extension of Peyré et al. (2016)’s scheme introduced by Séjourné et al. (2023b). For both unbalanced problems (EK) and (UEGW), instead of directly selecting λ_i , we introduce $\tau_i = \frac{\lambda_i}{\lambda_i + \varepsilon}$ s.t. we recover the hard marginal constraint for $\tau_i = 1$, when $\lambda_i \rightarrow +\infty$. We write $\tau = (\tau_1, \tau_2)$ accordingly.

2.2 CONDITIONAL FLOW MATCHING

Provided a prior distribution $\rho_0 \in \mathcal{M}_1^+(\mathbb{R}^d)$ and a time-dependent vector field v_t , one can define a probability path $(p_t)_{t \in [0,1]}$ starting from ρ_0 using the flow $(\phi_t)_{t \in [0,1]}$ induced by the ODE

$$\frac{d}{dt} \phi_t(\mathbf{z}) = v_t(\phi_t(\mathbf{z})), \quad \phi_0(\mathbf{z}) = \mathbf{z}, \quad (1)$$

by setting $p_t = \phi_t \# \rho_0$. In that case, we say that v_t generates the path p_t through the flow ϕ_t . Continuous Normalizing Flows (Chen et al., 2018) model the vector field with a neural network $v_{t,\theta}$, leading to a deep parametric model of the flow, which is trained to match a terminal condition defined by a target distribution $p_1 = \rho_1 \in \mathcal{M}_1^+(\mathbb{R}^d)$. (Conditional) Flow Matching (CFM) (Lipman et al., 2023) is a simulation-free technique to train CNFs by constructing probability paths between individual data samples $\mathbf{z}_0 \sim \rho_0$, $\mathbf{z}_1 \sim \rho_1$, and minimizing the loss

$$\mathcal{L}_{\text{CFM}}(\theta) = \mathbb{E}_{t \sim \mathcal{U}([0,1]), \mathbf{Z}_0 \sim \rho_0, \mathbf{Z}_1 \sim \rho_1} [\|v_{t,\theta}(t\mathbf{Z}_0 + (1-t)\mathbf{Z}_1) - (\mathbf{Z}_1 - \mathbf{Z}_0)\|_2^2]. \quad (2)$$

If this loss is 0, then $v_{t,\theta}$ generates a probability path between ρ_0 and ρ_1 , i.e. the induced flow satisfies $\phi_1 \# \rho_0 = \rho_1$ (Lipman et al., 2023)[Theorem 1]. To sample from ρ_1 , we solve the ODE (1) with $\mathbf{z}_0 \sim \rho_0$ and obtain $\phi_1(\mathbf{z}_0) \sim \rho_1$.

3 GENERATIVE ENTROPIC NEURAL OPTIMAL TRANSPORT

In this section, we introduce GENOT, a method to learn EOT couplings by learning their conditional distributions. In § (3.1), we first focus on the balanced OT case, when the source and the target

measures have the same mass, and show that GENOT can solve (EK) or (EGW). Second, in § (3.2), we extend GENOT to the unbalanced setting by loosening the conservation of mass constraint and defining U-GENOT, which can be used to solve problems (UEK) and (UEGW). Finally, in § 3.3, we highlight that GENOT also addresses a fused problem, combining (EK) and (EGW).

3.1 LEARNING ENTROPIC OPTIMAL COUPLINGS WITH GENOT

Let $\mu \in \mathcal{M}_1^+(\mathcal{X})$, $\nu \in \mathcal{M}_1^+(\mathcal{Y})$ and π_ε^* be an EOT coupling between μ and ν , which can be a solution of problem (EK) or (EGW). The measure disintegration theorem yields

$$d\pi_\varepsilon^*(\mathbf{x}, \mathbf{y}) = d\pi_{\varepsilon,1}^*(\mathbf{x}) d\pi_\varepsilon^*(\mathbf{y}|\mathbf{x}) = d\mu(\mathbf{x}) d\pi_\varepsilon^*(\mathbf{y}|\mathbf{x}). \quad (3)$$

Knowing μ , we can hence fully describe π_ε^* via the conditional distributions $(\pi_\varepsilon^*(\cdot|\mathbf{x}))_{\mathbf{x} \in \mathcal{X}}$. The latter are also of great practical interest, as they provide a way to transport a source sample $\mathbf{x} \sim \mu$ to the target domain \mathcal{Y} ; either *stochastically* by sampling $\mathbf{y}_1, \dots, \mathbf{y}_n \sim \pi_\varepsilon^*(\cdot|\mathbf{x})$, or *deterministically* by averaging over conditional samples:

$$T_\varepsilon(\mathbf{x}) := \mathbb{E}_{Y \sim \pi_\varepsilon^*(\cdot|\mathbf{x})}[Y] = \mathbb{E}_{(X,Y) \sim \pi_\varepsilon^*}[Y|X = \mathbf{x}]. \quad (4)$$

Moreover, we can compute any statistic of $\pi_\varepsilon^*(\cdot|\mathbf{x})$ to assess the uncertainty surrounding this prediction. In the following, we elaborate on our approach for calculating these conditional distributions.

Noise Outsourcing. Let $\rho \in \mathcal{M}_1^+(\mathcal{Z})$ be an atomless distribution on an arbitrary Borel space \mathcal{Z} , refer to as the noise. The noise outsourcing lemma (Kallenberg, 2002) states that there exists a collection of maps $\{T^*(\cdot|\mathbf{x})\}_{\mathbf{x} \in \mathcal{X}}$ with $T^*(\cdot|\mathbf{x}) : \mathcal{Z} \rightarrow \mathcal{Y}$ s.t. for each $\mathbf{x} \sim \mu$, $\pi_\varepsilon^*(\cdot|\mathbf{x}) = T^*(\cdot|\mathbf{x})\# \rho$. More precisely, if $\mathbf{x} \sim \mu$ and $\mathbf{z} \sim \rho$, then $\mathbf{y} = T^*(\mathbf{z}|\mathbf{x}) \sim \pi_\varepsilon^*(\cdot|\mathbf{x})$. Each $T^*(\cdot|\mathbf{x})$ generates a distribution from a point \mathbf{x} , by "outsourcing" the noise vectors $\mathbf{z} \sim \rho$. We refer to $\{T^*(\cdot|\mathbf{x})\}_{\mathbf{x} \in \mathcal{X}}$ as a collection of *optimal conditional generators* since they generate the conditional distributions of π_ε^* . Conversely, noise outsourcing provides a way to define neural couplings π_θ by parameterizing their conditional generators $\{T_\theta(\cdot|\mathbf{x})\}_{\mathbf{x} \in \mathcal{X}}$ with neural networks. To obtain $\pi_\theta \approx \pi_\varepsilon^*$, we then need $T_\theta(\cdot|\mathbf{x})$ to generate $\pi_\varepsilon^*(\cdot|\mathbf{x})$ by outsourcing the noise ρ , for any source sample $\mathbf{x} \sim \mu$.

Learning the Conditional Generators. In the following, we learn a collection of maps $\{T_\theta(\cdot|\mathbf{x})\}_{\mathbf{x} \in \mathcal{X}}$ fitting the constraint $T_\theta(\cdot|\mathbf{x})\# \rho \approx \pi_\varepsilon^*(\cdot|\mathbf{x})$ for any $\mathbf{x} \sim \mu$. Instead of directly modeling $T_\theta(\cdot|\mathbf{x})$ with a neural network, we employ the CFM framework discussed in § 2.2. To that end, we first set $\mathcal{Z} = \mathbb{R}^q$ and the noise $\rho = \mathcal{N}(0, I_q)$. We remind that q is the dimension of the target domain \mathcal{Y} . Then, we parameterize each $T_\theta(\cdot|\mathbf{x})$ implicitly as the flow induced by a neural vector field $v_{t,\theta}(\cdot|\mathbf{x}) : \mathbb{R}^q \rightarrow \mathbb{R}^q$. Namely $T_\theta(\cdot|\mathbf{x}) = \phi_1(\cdot|\mathbf{x})$ where $\phi_t(\cdot|\mathbf{x})$ solves

$$\frac{d}{dt} \phi_t(\mathbf{z}|\mathbf{x}) = v_{t,\theta}(\phi_t(\mathbf{z}|\mathbf{x})|\mathbf{x}), \quad \phi_0(\mathbf{z}|\mathbf{x}) = \mathbf{z}. \quad (5)$$

We stress that while $\mathbf{x} \in \mathcal{X} \subset \mathbb{R}^d$, the flow from ρ to $\pi_\varepsilon^*(\cdot|\mathbf{x})$ is defined on $\mathbb{R}^q \supset \mathcal{Y}$. Hence, we can map samples *within* the same space when $p = q$, but also *across* incomparable spaces when $p \neq q$. In particular, this allows us to solve the Gromov-Wasserstein problem (EGW). Thus, for each \mathbf{x} , we optimize $v_{t,\theta}(\cdot|\mathbf{x})$ by minimizing the CFM loss (2) with source ρ and target $\pi_\varepsilon^*(\cdot|\mathbf{x})$, i.e.

$$\mathbb{E}_{t \sim \mathcal{U}([0,1]), Z \sim \rho, Y \sim \pi_\varepsilon^*(\cdot|\mathbf{x})} [\|v_{t,\theta}((1-t)Z + tY|\mathbf{x}) - (Y - Z)\|_2^2]. \quad (6)$$

Averaging over source samples $\mathbf{x} \sim \mu$ and using Fubini's Theorem, we arrive at the GENOT loss

$$\mathcal{L}_{\text{GENOT}}(\theta) = \mathbb{E}_{t \sim \mathcal{U}([0,1]), Z \sim \rho, X \sim \mu, Y \sim \pi_\varepsilon^*(\cdot|X)} [\|v_{t,\theta}((1-t)Z + tY|X) - (Y - Z)\|_2^2]. \quad (7)$$

We optimize this loss by (i) estimating $\hat{\pi}_\varepsilon$ from samples $\mathbf{x}_1, \dots, \mathbf{x}_n \sim_{\text{i.i.d}} \mu$ and $\mathbf{y}_1, \dots, \mathbf{y}_n \sim_{\text{i.i.d}} \nu$, then (ii) sampling the estimated discrete conditional distributions. We detail our training procedure in algorithm 1. GENOT can be thought of as a conditional CFM model: For each \mathbf{x} , using CFM, we train a conditional vector field $v_{t,\theta}(\cdot|\mathbf{x})$ to generate $\pi_\varepsilon^*(\cdot|\mathbf{x})$ from the noise ρ .

Proposition 3.1 (GENOT recovers Optimal Conditional Generators.). *Suppose that $\mathcal{L}_{\text{GENOT}}(\theta) = 0$. Then the flows $\{\phi_t(\cdot|\mathbf{x})\}_{\mathbf{x} \in \mathcal{X}}$, induced by the velocity fields $\{v_{t,\theta}(\cdot|\mathbf{x})\}_{\mathbf{x} \in \mathcal{X}}$, are a collection of optimal conditional generators. Namely, if $\mathbf{x} \sim \mu$, $\mathbf{z} \sim \rho$ and $\mathbf{y} = \phi_1(\mathbf{z}|\mathbf{x})$ denotes the solution of the ODE (5), then $\mathbf{y} \sim \pi_\varepsilon^*(\cdot|\mathbf{x})$. Consequently, we recover π_ε^* .*

GENOT Addresses Any Cost. Thanks to Prop. 3.1, we can use GENOT to solve (EK) and (EGW) problems. In both cases, we do not impose any restrictions on the cost functions. We only need to be able to evaluate these costs on samples to estimate π_ε^* with a discrete solver. In particular, we can use costs that are implicitly defined and whose evaluation requires a non-differentiable sub-routine. For instance, recent works have proposed using the geodesic distance on the data manifold as cost, which can be approximated from samples by considering the shortest path distance on the k -nn graph induced by the Euclidean distance (Demetci et al., 2022). Using such data-driven cost functions is crucial for many applications where comparing samples via an ℓ_p distance is not meaningful, as in some single-cell genomic tasks (Huguet et al., 2022; Klein et al., 2023).

3.2 U-GENOT: EXTENSION TO THE UNBALANCED SETTING

Re-Balancing the UOT Problems. In its standard form, GENOT imposes the marginal constraints, so it cannot directly tackle the unbalanced problems (UEK) or (UEGW). However, these unbalanced problems can be *re-balanced*. In both Kantorovich and GW cases, we can show that the unbalanced EOT coupling $\pi_{\varepsilon,\tau}^*$ between $\mu \in \mathcal{M}^+(\mathcal{X})$ and $\nu \in \mathcal{M}^+(\mathcal{Y})$ actually solves a balanced EOT problem between its marginals, which are re-weighted versions of μ and ν that have the same mass.

Proposition 3.2 (Re-Balancing the unbalanced problems.). *Let $\pi_{\varepsilon,\tau}^*$ be an unbalanced EOT coupling, solution of (UEK) or (UEGW) between $\mu \in \mathcal{M}^+(\mathcal{X})$ and $\nu \in \mathcal{M}^+(\mathcal{Y})$. We note $\tilde{\mu} = p_1\# \pi_{\varepsilon,\tau}^*$ and $\tilde{\nu} = p_2\# \pi_{\varepsilon,\tau}^*$ its marginals. Then, in both cases, $\tilde{\mu}$ (resp. $\tilde{\nu}$) has a density w.r.t μ (resp. ν) i.e. it exists $\eta, \xi : \mathbb{R}^d \rightarrow \mathbb{R}^+$ s.t. $\tilde{\mu} = \eta \cdot \mu$ and $\tilde{\nu} = \xi \cdot \nu$. Moreover, $\tilde{\mu}$ and $\tilde{\nu}$ have the same mass and*

1. (Kantorovich) $\pi_{\varepsilon,\tau}^*$ solves the balanced problem (EK) between $\tilde{\mu}$ and $\tilde{\nu}$ with the same ε .
2. (Gromov-Wasserstein) Provided that c_X and c_Y are conditionally positive (or conditionally negative) kernels (see Def. B.1), $\pi_{\varepsilon,\tau}^*$ solves the balanced problem (EGW) between $\tilde{\mu}$ and $\tilde{\nu}$ with $\varepsilon' = m(\pi_{\varepsilon,\tau}^*) \varepsilon$, where $m(\pi_{\varepsilon,\tau}^*) = \pi_{\varepsilon,\tau}^*(\mathcal{X} \times \mathcal{Y})$ is the total mass of $\pi_{\varepsilon,\tau}^*$.

Remark. In various experimental settings, μ and ν have mass 1 and we impose one of the two hard marginal constraints, for instance on μ , by setting $\tau_1 = 1$. Then $\tilde{\nu}$ has also mass 1 and $m(\pi_{\varepsilon,\tau}^*) = 1$, so we keep the same regularization strength ε by re-balancing (UEGW).

Learning the Coupling and the Re-Weightings Simultaneously. Thanks to Prop. 3.2, we aim to (i) learn a balanced EOT coupling between $\tilde{\mu}$ and $\tilde{\nu}$ along with (ii) the re-weighting functions η, ξ . The latter are of key interest since they enable modeling the creation and destruction of mass. We can do both simultaneously by slightly adapting the GENOT procedure. More formally, we seek to optimize the U-GENOT loss

$$\begin{aligned} \mathcal{L}_{\text{U-GENOT}}(\theta) &= \mathbb{E}_{t \sim \mathcal{U}([0,1]), Z \sim \rho, X \sim \tilde{\mu}, Y \sim \pi_{\varepsilon,\tau}^*(\cdot|X)} [\|v_{t,\theta}(tZ + (1-t)Y|X) - (Y - Z)\|_2^2] \quad (\text{i}) \\ &\quad + \mathbb{E}_{X \sim \mu} [(\eta(X) - \eta_\theta(X))^2] + \mathbb{E}_{Y \sim \nu} [(\xi(Y) - \xi_\theta(Y))^2]. \quad (\text{ii}) \end{aligned}$$

As with GENOT, we simply need to estimate the unbalanced OT coupling $\hat{\pi}_{\varepsilon,\tau}$ from samples $\mathbf{x}_1, \dots, \mathbf{x}_n \sim_{\text{i.i.d}} \mu$ and $\mathbf{y}_1, \dots, \mathbf{y}_n \sim_{\text{i.i.d}} \nu$ to estimate that loss. We build upon theoretical insights from the Kantorovich case, which we extend in practice to the Gromov-Wasserstein case.

Proposition 3.3 (Estimation of the re-weightings.). *Let $\hat{\pi}_{\varepsilon,\tau}$ the solution of (UEK) computed on samples. Let $\mathbf{a} = \hat{\pi}_{\varepsilon,\tau} \mathbf{1}_n$ and $\mathbf{b} = \hat{\pi}_{\varepsilon,\tau}^\top \mathbf{1}_n$ be its marginal weights and let $\hat{\eta}_n(\mathbf{x}_i) := n a_i$ and $\hat{\xi}_n(\mathbf{y}_i) := n b_i$. Then, almost surely, $\hat{\eta}_n(\mathbf{x}_i) \rightarrow \eta(\mathbf{x}_i)$ and $\hat{\xi}_n(\mathbf{y}_i) \rightarrow \xi(\mathbf{y}_i)$.*

Using Prop. 3.2, $\hat{\pi}_{\varepsilon,\tau}$ is a balanced EOT coupling between its marginals, which are empirical approximations of $\tilde{\mu}$ and $\tilde{\nu}$. We hence estimate the term (i) of the loss as we do in the balanced case by sampling from the discrete conditional distribution. Furthermore, Prop.3.3 highlights that the estimation of $\hat{\pi}_{\varepsilon,\tau}$ also provides a consistent estimate of the re-weighting function evaluations at each \mathbf{x}_i and \mathbf{y}_i . This enables the estimation of the term (ii). Therefore, as with GENOT, each U-GENOT iteration only requires a call to a discrete solver. We detail our training procedure in algorithm 2.

3.3 COMBINING KANTOROVICH AND GROMOV-WASSERSTEIN TO THE FUSED SETTING

We show in § 3.1 and § 3.2 how to use our method to map samples within the same space, or across incomparable spaces, by solving (EK) or (EGW) and their unbalanced extensions. On the

other hand, there are cases where the source and the target domains are only *partially* incomparable, leading to a problem that combines both OT formulations (Vayer et al., 2018). Suppose that the source and target space can be decomposed as $\mathcal{X} = \Omega \times \tilde{\mathcal{X}}$ and $\mathcal{Y} = \Omega \times \tilde{\mathcal{Y}}$, respectively. Moreover, assume we are given an inter-domain cost $c : \Omega \times \Omega \rightarrow \mathbb{R}$ along with the intra-domain costs $c_{\tilde{\mathcal{X}}}, c_{\tilde{\mathcal{Y}}}$. The entropic fused-Gromov-Wassstein (FGW) problem can then be defined as

$$\min_{\pi \in \Pi(\mu, \nu)} \int_{((\Omega \times \tilde{\mathcal{X}}) \times (\Omega \times \tilde{\mathcal{Y}}))^2} L((\mathbf{u}, \mathbf{x}), (\mathbf{v}, \mathbf{y}), \mathbf{x}', \mathbf{y}') d\pi((\mathbf{u}, \mathbf{x}), (\mathbf{v}, \mathbf{y})) d\pi(\mathbf{x}', \mathbf{y}') + \varepsilon \text{KL}(\pi | \mu \otimes \nu), \quad \text{EFGW}$$

where $L((\mathbf{u}, \mathbf{x}), (\mathbf{v}, \mathbf{y}), \mathbf{x}', \mathbf{y}') := (1 - \alpha) c(\mathbf{u}, \mathbf{v}) + \alpha |c_{\tilde{\mathcal{X}}}(\mathbf{x}, \mathbf{x}') - c_{\tilde{\mathcal{Y}}}(\mathbf{y}, \mathbf{y}')|^2$ and $\alpha \in [0, 1]$ determines the influence of the components of the space decompositions. When $\alpha = 1$, we recover the pure GW setting. The above fused problem admits an unbalanced extension, which can be derived exactly in the same way as (UEGW) using the quadratic KL^\otimes (Thual et al., 2023).

(U-)GENOT Addresses the Fused Setting. Whether in the balanced or unbalanced setting, we can use our method to learn a specific coupling as soon as it can be estimated from samples. We stress that the discrete solvers we use for problems (EGW) and (UEGW) are still applicable in the fused setting. As a result, we can compute discrete fused couplings and then solve (EFGW) and its unbalanced counterpart with (U-)GENOT. To illustrate this idea more precisely, take a solution π_α^* of (EFGW). Learning π_α^* with our method amounts to training vector fields that are conditioned on pairs of modality from the source domain $v_{t,\theta}(\cdot, |\mathbf{u}, \mathbf{x})$, to sample pairs of modality from the target domain via the induced flow: $\mathbf{z} \sim \rho$, $\phi_1(\mathbf{z} | \mathbf{u}, \mathbf{x}) = (\mathbf{v}, \mathbf{y}) \sim \pi_\alpha^*(\cdot | \mathbf{u}, \mathbf{x})$. Given each term of the fused problem (EFGW), the sampled modalities (\mathbf{v}, \mathbf{y}) minimize transport cost quantified by c along the first modality, while being "isometric" w.r.t. $c_{\tilde{\mathcal{X}}}$ and $c_{\tilde{\mathcal{Y}}}$ on the second modality.

4 RELATED WORK

Neural EOT. While GENOT is the first model to learn neural EOT couplings in the (Fused) Gromov-Wasserstein or the unbalanced setting, various methods have been proposed in the (balanced) Kantorovich setting. The first class of methods solves the (EK) dual problem. While some of them (Genevay et al., 2019) do not allow direct sampling according to π_ε^* , Daniels et al. (2021) model the conditional distribution $\pi_\varepsilon^*(\cdot | \mathbf{x})$. However, this method is (i) costly as it employs Langevin sampling at inference time and (ii) numerically unstable as it requires the exponentiation of large numbers. Mokrov et al. (2023) proposed another approach modeling $\pi_\varepsilon^*(\cdot | \mathbf{x})$ leveraging energy-based models, but is computationally expensive since it relies on Langevin sampling in each training iteration. Other Kantorovich EOT solvers build upon the link between (EK) and the Schrödinger bridge (SB) problem. They model the EOT plan as a time-evolving stochastic process with fixed marginal constraints, endowed with learnable drift and diffusion terms (De Bortoli et al., 2021; Chen et al., 2021; Vargas et al., 2021; Gushchin et al., 2022). Although these methods have shown good performance on image data, they are very costly since they require simulation-based training. A recent line of work proposed to train such models in a completely simulation-free manner (Tong et al., 2023a;b; Shi et al., 2023; Liu et al., 2023) via score or flow matching. However, these methods can only be used for the squared Euclidean cost. Indeed, they rely on the fact that the marginals of the SB can be characterized as a mixture of Brownian bridges weighted by an EOT plan. However, this property is true only when we choose the Wiener process as a reference measure in the SB problem, which is limited to using $c(\mathbf{x}, \mathbf{y}) = \|\mathbf{x} - \mathbf{y}\|_2^2$ in (EK) (Léonard, 2013)[Eq. 1.2]. On the other hand, GENOT is the first neural EOT framework that can handle any cost function, even those defined implicitly, and whose evaluation requires a call to a non-differentiable sub-routine, like the geodesic distance on the data manifold. This point allows us to emphasize that our method fundamentally differs from theirs since we do not exploit the link between EOT and SB. Our approach is purely conditional and uses flow matching only as a powerful generative black box to generate each $\pi_\varepsilon^*(\cdot | \mathbf{x})$ from a ρ noise.

Computation of Neural Couplings. Another line of work considers computing neural couplings through the weak OT paradigm Korotin et al. (2022a;b); Asadulaev et al. (2022); Gazdieva et al. (2022), by solving a challenging min-max problem. However, (i) their method only enables mapping within the same space, (ii) in the balanced setting, and (iii) cannot handle EOT problems since they would require estimating the entropy of the neural coupling from samples at each iteration.

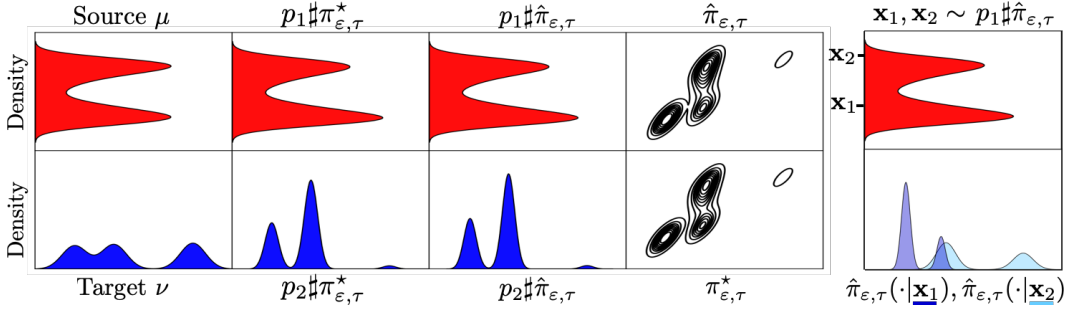


Figure 1: Prediction by UGENOT-K and ground truth of the unbalanced entropy-regularized transport plan between mixtures of Gaussians. The first column shows the source (top) and target (bottom) distribution. The second and third column show the marginal distributions of the true and the learnt transport plan, respectively. The fourth column compares the learnt (top) with the true (bottom) transport plan, while the fifth column plots conditional distributions. Here, $\varepsilon = 0.05$.

5 EXPERIMENTS

We demonstrate the applicability and versatility of the GENOT framework on toy data and single-cell data to map within the same space and across incomparable spaces. Metrics are discussed in appendix C and details on the single-cell datasets can be found in appendix D. Further experimental details or results for each experiment are reported in appendix E. Setups for competing methods are listed in appendix F. Details on the implementation of GENOT can be found in appendix G. We introduce the notation GENOT-K for the GENOT model solving problem (EK) while GENOT models solving the tasks (EGW) and (EFGW) are referred to as GENOT-GW and GENOT-FGW, respectively. The prefix U is used whenever consider an unbalanced problem, as described in § 3.2. Moreover, when reporting results based on the conditional mean of a GENOT model, we add the suffix *CM* to the model name. If not stated otherwise, we use the squared Euclidean distance as cost.

5.1 GENOT-K TO MAP WITHIN SPACES

U-GENOT-K on simulated data To visualize the capabilities of UGENOT-K to learn unbalanced entropy-regularized transport plans and rescaling functions, we compare its predictions with the OT plan obtained from a discrete EOT solver. Fig. 1 shows that the unbalanced entropy-regularized transport plan with $\varepsilon = 0.05$ and $\tau_1 = \tau_2 = 0.98$ between mixtures of Gaussians is accurately learnt by U-GENOT-K. The influence of the unbalancedness parameters τ_1, τ_2 is visualized in Fig. 7.

U-GENOT-K for modeling single-cell trajectories OT has been successfully applied to recover cellular trajectories in time-resolved single-cell data (Schiebinger et al., 2019). We apply GENOT-K to a dataset capturing gene expression of the developing mouse pancreas at embryonic days 14.5 and 15.5 (Bastidas-Ponce et al., 2019). We assess the fitting property of the learnt plan by computing the Sinkhorn divergence (Feydy et al., 2019a) between the predicted target distribution $p_2 \# \hat{\pi}_\varepsilon$ and the target distribution E.2. Fig. 8 shows that GENOT-K outperforms competing methods.

A key feature of all GENOT models is the ability to sample from the conditional distribution. Indeed, it is indispensable to stochastically model cellular trajectories, as cells are known to evolve non-deterministically (Elowitz et al., 2002). Following Gayoso et al. (2022), we compute $\text{cos-var}(\hat{\pi}_\varepsilon(\cdot|\mathbf{x})) = \text{Var}_{Y \sim \hat{\pi}_\varepsilon(\cdot|\mathbf{x})}[\text{cos-sim}(Y, \mathbb{E}_{Y \sim \hat{\pi}_\varepsilon(\cdot|\mathbf{x})}[Y])]$, where $\text{cos-sim}(\cdot, \cdot)$ denotes the cosine similarity, to assess the uncertainty of cell trajectories in the developing mouse pancreas (appendix C.1). We expect high uncertainty in cell types with fate decisions and low variance in mature cell types or cell types with a homogeneous descending population. Indeed, Fig. 2 and Fig. 9 show that GENOT-K helps to uncover lineage branching events.

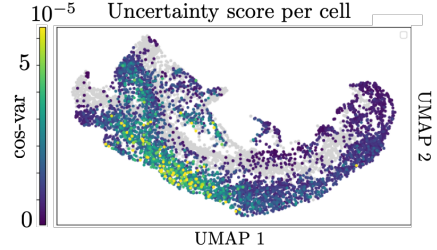


Figure 2: UMAP (McInnes et al., 2018) of the mouse pancreas development dataset colored by uncertainty per cell in the source distribution. Cells in the target distribution are colored in gray.

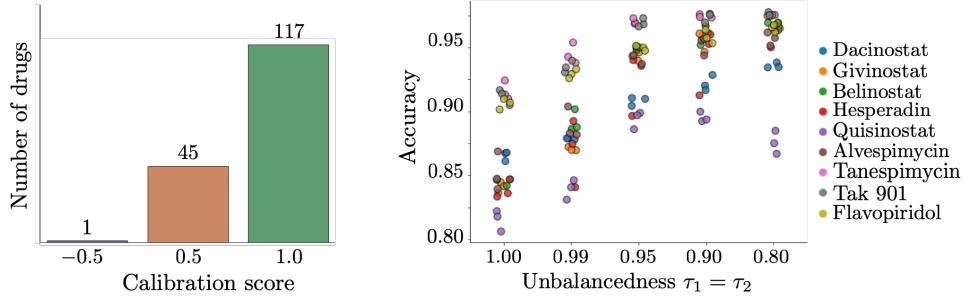


Figure 3: Left: Calibration score for the predictions of GENOT-K for modeling cellular responses to 163 cancer drugs (appendix C.1). Right: Accuracy of cellular response predictions of U-GENOT-K for different cancer drugs with varying unbalancedness parameter $\tau = \tau_1 = \tau_2$. For each τ , U-GENOT-K was run three times with different seeds.

The pancreas dataset considered so far subsets the original dataset to one cell lineage (endocrine) to prevent obtaining biologically implausible couplings. Indeed, table 1 shows that in the balanced case, the cell lineage transition score (see C.2) shows that only 66% of the cells are mapped to the correct lineage. By loosening the conservation of mass constraint, U-GENOT-K helps to counteract the distributional shift introduced by different proliferation rates of cells and experimental biases.

Prediction of cellular responses to drug perturbations with U-GENOT-K Neural OT maps have been successfully applied to model cellular responses to perturbations with deterministic neural OT maps (Bunne et al., 2021; Uscidda & Cuturi, 2023). Yet, these predictions lack information about the confidence of the model. GENOT enables to sample from the conditional distribution, which allows for uncertainty quantification. We consider single-cell RNAseq data measuring the response of cells to 163 different cancer drugs (Srivatsan et al., 2020). Each drug has been applied to a population of cells which can be partitioned into three different cell types. While there is no ground truth in the matching between unperturbed and perturbed cells due to the destructive nature of sequencing technologies, we know which unperturbed subset of cells is supposed to be mapped to which perturbed subset of cells. This allows us to define an accuracy metric (appendix C.2). For the uncertainty metric, we choose again cos-var. Fig. 3 shows that for 117 out of 163 drugs the model is perfectly well calibrated (appendix C.1), while it yields a negative correlation between error and uncertainty only for one drug.

To improve the accuracy of GENOT-K, we leverage its unbalanced formulation. Fig. 3 shows that allowing for mass variation improves the performance for nine different cancer drugs which are known to have a strong effect. Fig. 13 and 14 confirm the results visually.

5.2 GENOT-GW AND GENOT-FGW TO MAP ACROSS SPACES

GENOT-GW on simulated data.

We transport a Swiss roll in \mathbb{R}^3 to a spiral in \mathbb{R}^2 . Fig. 4 shows that GENOT-GW successfully mimics an isometric alignment. Here, we set $\varepsilon = 0.01$ and investigate its influence in more detail in Fig. 15.

GENOT-GW for translating modalities of single cells

The number of modalities which can be simultaneously measured in a single cell is limited due to technical limitations. Yet, it is important to match measurements of different modalities to obtain a more holistic view of the profile of a cell. The discrete GW formulation has been used to match measurements of cells in different modalities (Demetci et al., 2022). We use GENOT-GW to

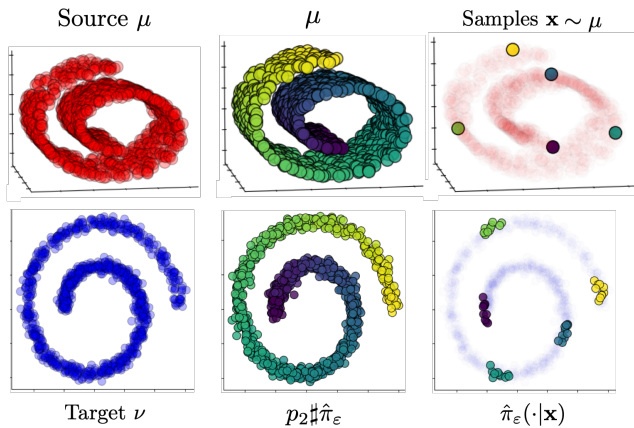


Figure 4: Mapping a Swiss roll in \mathbb{R}^3 (top left) to a spiral in \mathbb{R}^2 (bottom left). Center: Color code tracks where samples from the source (top) are mapped to (bottom). Right column: samples (top) and their conditional distributions.

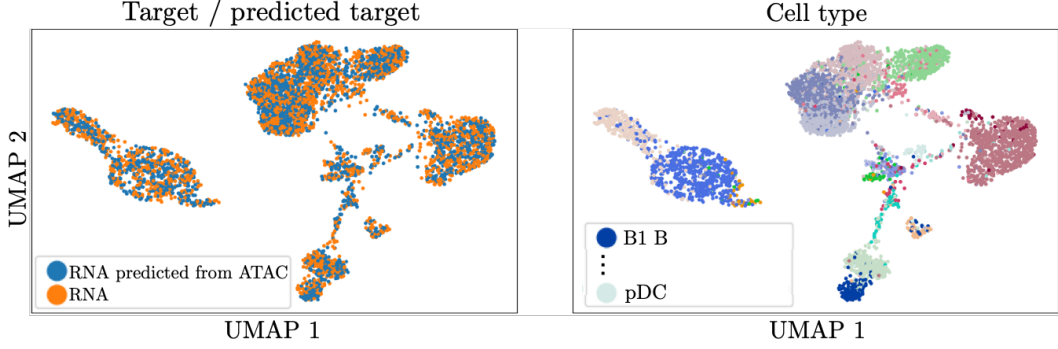


Figure 5: UMAP embedding of transported cells and cells in the target distribution (left), and jointly colored by cell type (right).

translate ATAC measurements to gene expression space on a bone marrow dataset (Luecken et al., 2021). As both modalities were measured in the same cell, the true match of each cell is known. We compare GENOT-GW with the discrete GW formulation (see F.2) and assess the performance with the FOSCTTM ("Fractions of Samples Closer to the True Match") score (see C.2). We leverage the flexibility of GENOT and choose an approximation of the geodesic distance (Crane et al., 2013) as it is known that Euclidean distances are often not meaningful in embeddings of single-cell measurements (Moon et al., 2018).

With respect to the FOSCTTM score, Fig. 6 shows three results. First, using a graph-based cost is crucial in higher dimensions. Second, out-of-sample prediction for discrete GW based on regression is competitive for lower dimensions, but not for high-dimensional spaces. Third, taking the conditional mean as prediction improves the result with respect to the FOSCTTM score. Regarding the distributional fitting property the striking superiority of GENOT models is unmistakable. Crucially, Fig. 6 shows that the fitting property of GENOT models is not affected by the cost.

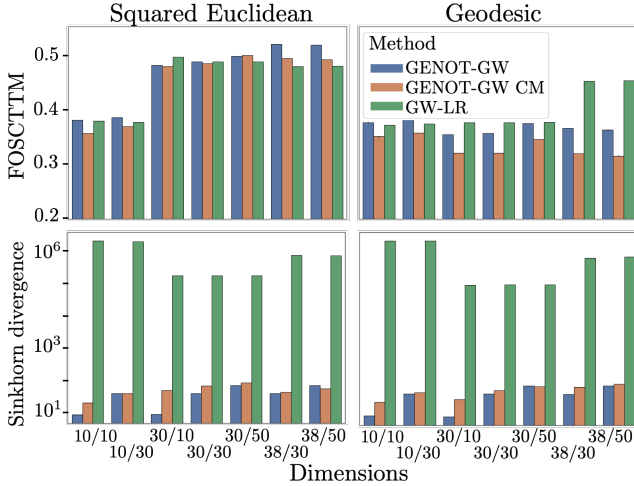


Figure 6: Benchmark (mean and std across three runs) of GENOT-GW models against discrete GW (GW-LR, appendix F) on translating cells between ATAC space of dimension d_1 and RNA space of dimension d_2 for experiment d_1/d_2 . Performance is measured with the FOSCTTM score (appendix C.2) and the Sinkhorn divergence between target and predicted target distribution. While on the left, we learn the EOT coupling for the squared Euclidean cost, we use the geodesic cost on the right (Crane et al., 2013).

fitting property, while the separation into cell types on the right confirms the optimality of the learnt coupling. See figures 19 and 20 for further visualizations.

GENOT-FGW improves modality translation of single cells

As the predictions yielded by GW-based models are not satisfactory, we introduce a novel method for translating between ATAC and RNA measurements by extending the model proposed by Demetci et al. (2022) to the fused setting. Therefore, we infer approximate gene expression from the ATAC measurements using gene activity (Stuart et al., 2021). We construct a joint space of the two modalities using a conditional VAE (Lopez et al., 2018a). Fig. 16 shows that the additional fused term helps to obtain a significantly better alignment compared to GENOT-GW, with the best GENOT-FGW CM model (weight parameter $\alpha = 0.7$) attaining a FOSCTTM score of below 0.05. It is important to note that incorporating the GW terms is necessary for attaining good results as discussed in appendix E.3. Fig. 5 visualizes the push-forward of the learnt coupling. The intertwining of samples of the target and the predicted target in the left panel visualizes the distribution

When aligning multiple modalities of single cells, we cannot assume to have the same proportion of cell types in both datasets, for example due to experimental biases caused by sequencing technologies. We simulate this setting by removing cells belonging to either of the cell types *Proerythroblasts*, *Erythroblasts* or *Normoblasts* in the source distribution. Table 3 shows that U-GENOT-FGW preserves high accuracy while learning meaningful rescaling functions.

Conclusion. We introduce GENOT, a versatile neural OT framework to learn cost-efficient stochastic maps within the same space and/or across incomparable spaces. GENOT is flexible to the extent that the mass conservation constraint can be loosened, and provides tools to sample targets from an input. GENOT can be used within a wide array of tasks in single-cell biology.

6 ACKNOWLEDGEMENTS

Co-funded by the European Union (ERC, DeepCell - 101054957). Views and opinions expressed are however those of the author(s) only and do not necessarily reflect those of the European Union or the European Research Council. Neither the European Union nor the granting authority can be held responsible for them. F.J.T. consults for Immunai Inc., Singularity Bio B.V., CytoReason Ltd, Cellarity, and has ownership interest in Dermagnostix GmbH and Cellarity.

REFERENCES

- David Alvarez-Melis and Tommi S Jaakkola. Gromov-wasserstein alignment of word embedding spaces. *arXiv preprint arXiv:1809.00013*, 2018.
- Arip Asadulaev, Alexander Korotin, Vage Egiazarian, and Evgeny Burnaev. Neural optimal transport with general cost functionals, 2022. URL <https://arxiv.org/abs/2205.15403>.
- Yogesh Balaji, Rama Chellappa, and Soheil Feizi. Robust optimal transport with applications in generative modeling and domain adaptation. *Advances in Neural Information Processing Systems*, 33:12934–12944, 2020.
- Aimée Bastidas-Ponce, Sophie Tritschler, Leander Dony, Katharina Scheibner, Marta Tarquis-Medina, Ciro Salinno, Silvia Schirge, Ingo Burtcher, Anika Böttcher, Fabian J Theis, et al. Comprehensive single cell mrna profiling reveals a detailed roadmap for pancreatic endocrinogenesis. *Development*, 146(12):dev173849, 2019.
- James Bradbury, Roy Frostig, Peter Hawkins, Matthew James Johnson, Chris Leary, Dougal Maclaurin, George Necula, Adam Paszke, Jake VanderPlas, Skye Wanderman-Milne, and Qiao Zhang. JAX: composable transformations of Python+NumPy programs, 2018. URL <http://github.com/google/jax>.
- Charlotte Bunne, Stefan G Stark, Gabriele Gut, Jacobo Sarabia del Castillo, Kjong-Van Lehmann, Lucas Pelkmans, Andreas Krause, and Gunnar Ratsch. Learning Single-Cell Perturbation Responses using Neural Optimal Transport. *bioRxiv*, 2021.
- Charlotte Bunne, Andreas Krause, and Marco Cuturi. Supervised training of conditional monge maps. In *Advances in Neural Information Processing Systems (NeurIPS)*, 2022.
- Ricky TQ Chen, Yulia Rubanova, Jesse Bettencourt, and David K Duvenaud. Neural ordinary differential equations. *Advances in neural information processing systems*, 31, 2018.
- Tianrong Chen, Guan-Hong Liu, and Evangelos A Theodorou. Likelihood training of schrödinger bridge using forward-backward sdes theory. *arXiv preprint arXiv:2110.11291*, 2021.
- Lenaïc Chizat, Gabriel Peyré, Bernhard Schmitzer, and François-Xavier Vialard. Unbalanced optimal transport: geometry and Kantorovich formulation. *Journal of Functional Analysis*, 274(11): 3090–3123, 2018.
- Keenan Crane, Clarisse Weischedel, and Max Wardetzky. Geodesics in heat: A new approach to computing distance based on heat flow. *ACM Transactions on Graphics (TOG)*, 32(5):1–11, 2013.

- Marco Cuturi. Sinkhorn Distances: Lightspeed Computation of Optimal Transport. In *Advances in Neural Information Processing Systems (NeurIPS)*, volume 26, 2013.
- Marco Cuturi, Laetitia Meng-Papaxanthos, Yingtao Tian, Charlotte Bunne, Geoff Davis, and Olivier Teboul. Optimal Transport Tools (OTT): A JAX Toolbox for all things Wasserstein. *arXiv Preprint arXiv:2201.12324*, 2022.
- Max Daniels, Tyler Maunu, and Paul Hand. Score-based generative neural networks for large-scale optimal transport. *Advances in neural information processing systems*, 34:12955–12965, 2021.
- Valentin De Bortoli, James Thornton, Jeremy Heng, and Arnaud Doucet. Diffusion schrödinger bridge with applications to score-based generative modeling. *Advances in Neural Information Processing Systems*, 34:17695–17709, 2021.
- Pinar Demetci, Rebecca Santorella, Björn Sandstede, William Stafford Noble, and Ritambhara Singh. Scot: single-cell multi-omics alignment with optimal transport. *Journal of Computational Biology*, 29(1):3–18, 2022.
- Théo Dumont, Théo Lacombe, and François-Xavier Vialard. On the existence of monge maps for the gromov-wasserstein problem. 2022.
- Michael B Elowitz, Arnold J Levine, Eric D Siggia, and Peter S Swain. Stochastic gene expression in a single cell. *Science*, 297(5584):1183–1186, 2002.
- Luca Vincent Eyring, Dominik Klein, Giovanni Palla, Soeren Becker, Philipp Weiler, Niki Kilbertus, and Fabian J. Theis. Modeling single-cell dynamics using unbalanced parameterized monge maps. *bioRxiv*, 2022. doi: 10.1101/2022.10.04.510766. URL <https://www.biorxiv.org/content/early/2022/10/05/2022.10.04.510766>.
- Jiaojiao Fan, Amirhossein Taghvaei, and Yongxin Chen. Scalable computations of wasserstein barycenter via input convex neural networks. *arXiv preprint arXiv:2007.04462*, 2020.
- Jean Feydy, Thibault Séjourné, François-Xavier Vialard, Shun-Ichi Amari, Alain Trounev, and Gabriel Peyré. Interpolating between Optimal Transport and MMD using Sinkhorn Divergences. In *International Conference on Artificial Intelligence and Statistics (AISTATS)*, volume 22, 2019a.
- Jean Feydy, Thibault Séjourné, François-Xavier Vialard, Shun-ichi Amari, Alain Trounev, and Gabriel Peyré. Interpolating between optimal transport and mmd using sinkhorn divergences. In *The 22nd International Conference on Artificial Intelligence and Statistics*, pp. 2681–2690. PMLR, 2019b.
- Charlie Frogner, Chiyan Zhang, Hossein Mobahi, Mauricio Araya, and Tomaso A Poggio. Learning with a wasserstein loss. *Advances in neural information processing systems*, 28, 2015.
- Adam Gayoso, Philipp Weiler, Mohammad Lotfollahi, Dominik Klein, Justin Hong, Aaron M Streets, Fabian J Theis, and Nir Yosef. Deep generative modeling of transcriptional dynamics for rna velocity analysis in single cells. *bioRxiv*, pp. 2022–08, 2022.
- Milena Gazdieva, Litu Rout, Alexander Korotin, Andrey Kravchenko, Alexander Filippov, and Evgeny Burnaev. An optimal transport perspective on unpaired image super-resolution, 2022. URL <https://arxiv.org/abs/2202.01116>.
- Aude Genevay, Lénaïc Chizat, Francis Bach, Marco Cuturi, and Gabriel Peyré. Sample Complexity of Sinkhorn Divergences. In *International Conference on Artificial Intelligence and Statistics (AISTATS)*, volume 22, 2019.
- Nikita Gushchin, Alexander Kolesov, Alexander Korotin, Dmitry Vetrov, and Evgeny Burnaev. Entropic neural optimal transport via diffusion processes. *arXiv preprint arXiv:2211.01156*, 2022.
- Lukas Heumos, Anna C Schaar, Christopher Lance, Anastasia Litinetskaya, Felix Drost, Luke Zappia, Malte D Lücken, Daniel C Strobl, Juan Henao, Fabiola Curion, et al. Best practices for single-cell analysis across modalities. *Nature Reviews Genetics*, pp. 1–23, 2023.

- Guillaume Huguet, Alexander Tong, María Ramos Zapatero, Guy Wolf, and Smita Krishnaswamy. Geodesic sinkhorn: optimal transport for high-dimensional datasets. *arXiv preprint arXiv:2211.00805*, 2022.
- Olav Kallenberg. *Foundations of Modern Probability*. Springer, 2002. URL <https://link.springer.com/book/10.1007/978-3-030-61871-1>.
- L Kantorovich. On the transfer of masses (in russian). In *Doklady Akademii Nauk*, volume 37, pp. 227, 1942.
- Dominik Klein, Giovanni Palla, Marius Lange, Michal Klein, Zoe Piran, Manuel Gander, Laetitia Meng-Papaxanthos, Michael Sterr, Aimee Bastidas-Ponce, Marta Tarquis-Medina, et al. Mapping cells through time and space with moscot. *bioRxiv*, pp. 2023–05, 2023.
- Alexander Korotin, Vage Egiazarian, Arip Asadulaev, Alexander Safin, and Evgeny Burnaev. Wasserstein-2 generative networks. In *International Conference on Learning Representations*, 2020.
- Alexander Korotin, Daniil Selikhanovych, and Evgeny Burnaev. Kernel neural optimal transport. 2022a. doi: 10.48550/ARXIV.2205.15269. URL <https://arxiv.org/abs/2205.15269>.
- Alexander Korotin, Daniil Selikhanovych, and Evgeny Burnaev. Neural optimal transport. 2022b. doi: 10.48550/ARXIV.2201.12220. URL <https://arxiv.org/abs/2201.12220>.
- Marius Lange, Zoe Piran, Michal Klein, Bastiaan Spanjaard, Dominik Klein, Jan Philipp Junker, Fabian J Theis, and Mor Nitzan. Mapping lineage-traced cells across time points with moslin. *bioRxiv*, pp. 2023–04, 2023.
- Matthias Liero, Alexander Mielke, and Giuseppe Savaré. Optimal entropy-transport problems and a new hellinger–kantorovich distance between positive measures. *Inventiones Mathematicae*, 211(3):969–1117, 2018.
- Yaron Lipman, Ricky T. Q. Chen, Heli Ben-Hamu, Maximilian Nickel, and Matt Le. Flow matching for generative modeling, 2023.
- Guan-Hong Liu, Arash Vahdat, De-An Huang, Evangelos A. Theodorou, Weili Nie, and Anima Anandkumar. \mathbb{I}^2 sb: Image-to-image schrödinger bridge, 2023.
- Romain Lopez, Jeffrey Regier, Michael B Cole, Michael I Jordan, and Nir Yosef. Deep generative modeling for single-cell transcriptomics. *Nature methods*, 15(12):1053–1058, 2018a.
- Romain Lopez, Jeffrey Regier, Michael B Cole, Michael I Jordan, and Nir Yosef. Deep generative modeling for single-cell transcriptomics. *Nature methods*, 15(12), 2018b.
- Frederike Lübeck, Charlotte Bunne, Gabriele Gut, Jacobo Sarabia del Castillo, Lucas Pelkmans, and David Alvarez-Melis. Neural unbalanced optimal transport via cycle-consistent semi-couplings. *arXiv preprint arXiv:2209.15621*, 2022.
- Malte D Luecken, Daniel Bernard Burkhardt, Robrecht Cannoodt, Christopher Lance, Aditi Agrawal, Hananeh Aliee, Ann T Chen, Louise Deconinck, Angela M Detweiler, Alejandro A Granados, et al. A sandbox for prediction and integration of dna, rna, and proteins in single cells. In *Thirty-fifth conference on neural information processing systems datasets and benchmarks track (Round 2)*, 2021.
- Christian Léonard. A survey of the schrödinger problem and some of its connections with optimal transport, 2013.
- Ashok Makkuva, Amirhossein Taghvaei, Sewoong Oh, and Jason Lee. Optimal transport mapping via input convex neural networks. In *International Conference on Machine Learning (ICML)*, volume 37, 2020.
- Leland McInnes, John Healy, and James Melville. Umap: Uniform manifold approximation and projection for dimension reduction. *arXiv preprint arXiv:1802.03426*, 2018.

- Facundo Mémoli. Gromov–wasserstein distances and the metric approach to object matching. *Foundations of computational mathematics*, 11:417–487, 2011.
- Petr Mokrov, Alexander Korotin, and Evgeny Burnaev. Energy-guided entropic neural optimal transport. *arXiv preprint arXiv:2304.06094*, 2023.
- Kevin R Moon, Jay S Stanley III, Daniel Burkhardt, David van Dijk, Guy Wolf, and Smita Krishnaswamy. Manifold learning-based methods for analyzing single-cell rna-sequencing data. *Current Opinion in Systems Biology*, 7:36–46, 2018.
- Maksim Nekrashevich, Alexander Korotin, and Evgeny Burnaev. Neural gromov-wasserstein optimal transport. *arXiv preprint arXiv:2303.05978*, 2023.
- Mor Nitzan, Nikos Karaikos, Nir Friedman, and Nikolaus Rajewsky. Gene expression cartography. *Nature*, 576(7785):132–137, 2019.
- Marcel Nutz. Introduction to entropic optimal transport.
- Gabriel Peyré, Marco Cuturi, and Justin Solomon. Gromov-wasserstein averaging of kernel and distance matrices. In *International Conference on Machine Learning*, pp. 2664–2672, 2016.
- Filippo Santambrogio. Optimal Transport for Applied Mathematicians. *Birkhäuser, NY*, 55(58-63): 94, 2015.
- Meyer Scetbon, Marco Cuturi, and Gabriel Peyré. Low-rank sinkhorn factorization. In *International Conference on Machine Learning*, pp. 9344–9354. PMLR, 2021.
- Meyer Scetbon, Gabriel Peyré, and Marco Cuturi. Linear-time gromov wasserstein distances using low rank couplings and costs. In *International Conference on Machine Learning*, pp. 19347–19365. PMLR, 2022.
- Geoffrey Schiebinger, Jian Shu, Marcin Tabaka, Brian Cleary, Vidya Subramanian, Aryeh Solomon, Joshua Gould, Siyan Liu, Stacie Lin, Peter Berube, et al. Optimal-Transport Analysis of Single-Cell Gene Expression Identifies Developmental Trajectories in Reprogramming. *Cell*, 176(4), 2019.
- Thibault Séjourné, François-Xavier Vialard, and Gabriel Peyré. The unbalanced gromov wasserstein distance: Conic formulation and relaxation. *Advances in Neural Information Processing Systems*, 34:8766–8779, 2021.
- Yuyang Shi, Valentin De Bortoli, Andrew Campbell, and Arnaud Doucet. Diffusion schrödinger bridge matching. *arXiv preprint arXiv:2303.16852*, 2023.
- Sanjay R Srivatsan, José L McFaline-Figueroa, Vijay Ramani, Lauren Saunders, Junyue Cao, Jonathan Packer, Hannah A Pliner, Dana L Jackson, Riza M Daza, Lena Christiansen, et al. Massively multiplex chemical transcriptomics at single-cell resolution. *Science*, 367(6473), 2020.
- Tim Stuart, Avi Srivastava, Shaista Madad, Caleb A Lareau, and Rahul Satija. Single-cell chromatin state analysis with signac. *Nature methods*, 18(11):1333–1341, 2021.
- Karl-Theodor Sturm. The space of spaces: curvature bounds and gradient flows on the space of metric measure spaces, 2020.
- Thibault Séjourné, Gabriel Peyré, and François-Xavier Vialard. Unbalanced optimal transport, from theory to numerics, 2023a.
- Thibault Séjourné, François-Xavier Vialard, and Gabriel Peyré. The unbalanced gromov wasserstein distance: Conic formulation and relaxation, 2023b.
- Alexis Thual, Huy Tran, Tatiana Zemskova, Nicolas Courty, Rémi Flamary, Stanislas Dehaene, and Bertrand Thirion. Aligning individual brains with fused unbalanced gromov-wasserstein, 2023.
- Alexander Tong, Jessie Huang, Guy Wolf, David Van Dijk, and Smita Krishnaswamy. TrajectoryNet: A Dynamic Optimal Transport Network for Modeling Cellular Dynamics. In *International Conference on Machine Learning (ICML)*, 2020.

- Alexander Tong, Nikolay Malkin, Kilian Fatras, Lazar Atanackovic, Yanlei Zhang, Guillaume Huguet, Guy Wolf, and Yoshua Bengio. Simulation-free schrödinger bridges via score and flow matching. *arXiv preprint arXiv:2307.03672*, 2023a.
- Alexander Tong, Nikolay Malkin, Guillaume Huguet, Yanlei Zhang, Jarrod Rector-Brooks, Kilian Fatras, Guy Wolf, and Yoshua Bengio. Conditional flow matching: Simulation-free dynamic optimal transport. *arXiv preprint arXiv:2302.00482*, 2023b.
- Théo Uscidda and Marco Cuturi. The monge gap: A regularizer to learn all transport maps, 2023.
- Francisco Vargas, Pierre Thodoroff, Austen Lamacraft, and Neil Lawrence. Solving schrödinger bridges via maximum likelihood. *Entropy*, 23(9):1134, 2021.
- Titouan Vayer, Laetitia Chapel, Rémi Flamary, Romain Tavenard, and Nicolas Courty. Optimal transport for structured data with application on graphs. *arXiv preprint arXiv:1805.09114*, 2018.
- Karren D Yang and Caroline Uhler. Scalable Unbalanced Optimal Transport using Generative Adversarial Networks. *International Conference on Learning Representations (ICLR)*, 2019.
- Ron Zeira, Max Land, Alexander Strzalkowski, and Benjamin J Raphael. Alignment and integration of spatial transcriptomics data. *Nature Methods*, 19(5):567–575, 2022.

APPENDIX

A ALGORITHMS

Algorithm 1 GENOT

Require: Source distribution μ ; target distribution ν ; batch size n ; number of (per \mathbf{x}) conditional sample k ; number of iterations T_{iter} , entropic regularization strength ε , discrete solver $\text{Solver}_\varepsilon$ to estimate π_ε^* from samples, parameterized time-dependent velocity field $v_{t,\theta}$.

- 1: **for** $t = 1, \dots, T_{\text{iter}}$ **do**
- 2: Sample batches $\mathbf{x}_1, \dots, \mathbf{x}_n \sim \text{i.i.d } \mu$ and $\mathbf{y}_1, \dots, \mathbf{y}_n \sim \text{i.i.d } \nu$.
- 3: Compute $\hat{\pi}_\varepsilon = \text{Solver}_\varepsilon(\{\mathbf{x}_i\}_{i=1}^n, \{\mathbf{y}_i\}_{i=1}^n) \in \mathbb{R}_+^{n \times n}$.
- 4: **for** $i = 1, \dots, n$ **do**
- 5: Sample from the discrete conditional distribution $\hat{\mathbf{y}}_{i,1}, \dots, \hat{\mathbf{y}}_{i,k} \sim \hat{\pi}_\varepsilon(\cdot | \mathbf{x}_i)$.
- 6: Sample noise vectors $\mathbf{z}_{i,1}, \dots, \mathbf{z}_{i,k} \sim \rho$.
- 7: Sample time-steps $\mathbf{t}_{i,1}, \dots, \mathbf{t}_{i,k} \sim \mathcal{U}([0, 1])$.
- 8: **end for**
- 9: Estimate GENOT loss:

$$\hat{\mathcal{L}}_{\text{GENOT}}(\theta) \leftarrow \frac{1}{n} \sum_{i=1}^n \frac{1}{k} \sum_{j=1}^k \|v_{t,\theta}(\mathbf{t}_{i,j} \mathbf{z}_{i,j} + (1 - \mathbf{t}_{i,j}) \hat{\mathbf{y}}_{i,j} | \mathbf{x}_i) - (\hat{\mathbf{y}}_{i,j} - \mathbf{z}_{i,j})\|_2^2.$$

- 10: Update θ to minimize $\hat{\mathcal{L}}_{\text{GENOT}}$.
- 11: **end for**

Algorithm 2 U-GENOT

Require: Source distribution μ ; target distribution ν ; batch size n ; number of (per \mathbf{x}) conditional sample k ; number of iterations T_{iter} , entropic regularization strength ε , left and right unbalancedness parameter $\tau = (\tau_1, \tau_2)$, discrete solver $\text{Solver}_{\varepsilon,\tau}$ to estimate $\pi_{\varepsilon,\tau}^*$ from samples, parameterized time-dependent velocity field $v_{t,\theta}$, parameterized re-weighting functions η_θ, ξ_θ .

- 1: **for** $t = 1, \dots, T_{\text{iter}}$ **do**
- 2: Sample batches $\mathbf{x}_1, \dots, \mathbf{x}_n \sim \text{i.i.d } \mu$ and $\mathbf{y}_1, \dots, \mathbf{y}_n \sim \text{i.i.d } \nu$.
- 3: Compute $\hat{\pi}_{\varepsilon,\tau} \leftarrow \text{Solver}_{\varepsilon,\tau}(\{\mathbf{x}_i\}_{i=1}^n, \{\mathbf{y}_i\}_{i=1}^n)$
- 4: Set the marginal weights: $\mathbf{a} \leftarrow \hat{\pi}_{\varepsilon,\tau} \mathbf{1}_n$ and $\mathbf{b} \leftarrow \hat{\pi}_{\varepsilon,\tau}^\top \mathbf{1}_n$.
- 5: Set $\tilde{\mu}_n \leftarrow \sum_{i=1}^n a_i \delta_{\mathbf{x}_i}$ the left marginal of $\hat{\pi}_{\varepsilon,\tau}$.
- 6: Sample $\tilde{\mathbf{x}}_1, \dots, \tilde{\mathbf{x}}_n \sim \tilde{\mu}_n$.
- 7: **for** $i = 1, \dots, n$ **do**
- 8: Sample from the discrete conditional distribution $\hat{\mathbf{y}}_{i,1}, \dots, \hat{\mathbf{y}}_{i,k} \sim \hat{\pi}_{\varepsilon,\tau}(\cdot | \tilde{\mathbf{x}}_i)$.
- 9: Sample noise vectors $\mathbf{z}_{i,1}, \dots, \mathbf{z}_{i,k} \sim \rho$.
- 10: Sample time-steps $\mathbf{t}_{i,1}, \dots, \mathbf{t}_{i,k} \sim \mathcal{U}([0, 1])$.
- 11: **end for**
- 12: Estimate re-weightings: $(\hat{\eta}_n(\mathbf{x}_1), \dots, \hat{\eta}_n(\mathbf{x}_n)) \leftarrow n \mathbf{a}$ and $(\hat{\xi}_n(\mathbf{y}_1), \dots, \hat{\xi}_n(\mathbf{y}_n)) \leftarrow n \mathbf{b}$.
- 13: Estimate U-GENOT loss:

$$\begin{aligned} \hat{\mathcal{L}}_{\text{U-GENOT}}(\theta) \leftarrow & \frac{1}{n} \sum_{i=1}^n \frac{1}{k} \sum_{j=1}^k \|v_{t,\theta}(\mathbf{t}_{i,j} \mathbf{z}_{i,j} + (1 - \mathbf{t}_{i,j}) \hat{\mathbf{y}}_{i,j} | \tilde{\mathbf{x}}_i) - (\hat{\mathbf{y}}_{i,j} - \mathbf{z}_{i,j})\|_2^2 \\ & + \frac{1}{n} \sum_{i=1}^n (\eta_\theta(\mathbf{x}_i) - \hat{\eta}(\mathbf{x}_i))^2 + \frac{1}{n} \sum_{i=1}^n (\xi_\theta(\mathbf{y}_i) - \hat{\xi}(\mathbf{y}_i))^2 \end{aligned}$$

- 14: Update θ to minimize $\hat{\mathcal{L}}_{\text{U-GENOT}}$.
- 15: **end for**

B PROOFS

B.1 PROOFS OF § 3

Proposition 3.1 (GENOT recovers Optimal Conditional Generators.). *Suppose that $\mathcal{L}_{\text{GENOT}}(\theta) = 0$. Then the flows $\{\phi_1(\cdot|\mathbf{x})\}_{\mathbf{x} \in \mathcal{X}}$, induced by the velocity fields $\{v_{t,\theta}(\cdot|\mathbf{x})\}_{\mathbf{x} \in \mathcal{X}}$, are a collection of optimal conditional generators. Namely, if $\mathbf{x} \sim \mu$, $\mathbf{z} \sim \rho$ and $\mathbf{y} = \phi_1(\mathbf{z}|\mathbf{x})$ denotes the solution of the ODE (5), then $\mathbf{y} \sim \pi_\varepsilon^*(\cdot|\mathbf{x})$. Consequently, we recover π_ε^* .*

Proof. This result follows directly from the construction of the loss. Suppose that $\mathcal{L}_{\text{GENOT}}(\theta) = 0$. By Fubini's Theorem, this implies that:

$$\mathbb{E}_{X \sim \mu} \mathbb{E}_{t \sim \mathcal{U}([0,1]), Z \sim \rho, Y \sim \pi_\varepsilon^*(\cdot|\mathbf{x})} [\|v_{t,\theta}(tZ + (1-t)Y|X) - (Y - Z)\|_2^2] = 0. \quad (8)$$

Since it is positive, the function

$$\ell : \mathbf{x} \mapsto \mathbb{E}_{t \sim \mathcal{U}([0,1]), Z \sim \rho, Y \sim \pi_\varepsilon^*(\cdot|\mathbf{x})} [\|v_{t,\theta}(tZ + (1-t)Y|\mathbf{x}) - (Y - Z)\|_2^2]$$

is therefore zero μ -a.e. which means that for any source sample $\mathbf{x} \sim \mu$, one has $\ell(\mathbf{x}) = 0$. Moreover, $\ell(\mathbf{x})$ is the CFM loss with source ρ and target $\pi_\varepsilon^*(\cdot|\mathbf{x})$, applied to the vector field $v_{t,\theta}(\cdot|\mathbf{x})$. Therefore, $\ell(\mathbf{x}) = 0$ implies that $v_{t,\theta}(\cdot|\mathbf{x})$ generates a probability path between ρ and $\pi_\varepsilon^*(\cdot|\mathbf{x})$ thanks to (Lipman et al., 2023)[Theorem 1], which means that if $\phi_t(\cdot|\mathbf{x})$ is the flow induced by $v_{t,\theta}(\cdot|\mathbf{x})$, $\phi_1(\cdot|\mathbf{x}) \# \rho = \pi_\varepsilon^*(\cdot|\mathbf{x})$. Therefore, $\{\phi_1(\cdot|\mathbf{x})\}_{\mathbf{x} \in \mathcal{X}}$ is a collection of optimal conditional generator. \square

Proposition 3.2 (Re-Balancing the unbalanced problems.). *Let $\pi_{\varepsilon,\tau}^*$ be an unbalanced EOT coupling, solution of (UEK) or (UEGW) between $\mu \in \mathcal{M}^+(\mathcal{X})$ and $\nu \in \mathcal{M}^+(\mathcal{Y})$. We note $\tilde{\mu} = p_1 \# \pi_{\varepsilon,\tau}^*$ and $\tilde{\nu} = p_2 \# \pi_{\varepsilon,\tau}^*$ its marginals. Then, in both cases, $\tilde{\mu}$ (resp. $\tilde{\nu}$) has a density w.r.t μ (resp. ν) i.e. it exists $\eta, \xi : \mathbb{R}^d \rightarrow \mathbb{R}^+$ s.t. $\tilde{\mu} = \eta \cdot \mu$ and $\tilde{\nu} = \xi \cdot \nu$. Moreover, $\tilde{\mu}$ and $\tilde{\nu}$ have the same mass and*

1. (Kantorovich) $\pi_{\varepsilon,\tau}^*$ solves the balanced problem (EK) between $\tilde{\mu}$ and $\tilde{\nu}$ with the same ε .
2. (Gromov-Wasserstein) Provided that $c_{\mathcal{X}}$ and $c_{\mathcal{Y}}$ are conditionally positive (or conditionally negative) kernels (see Def. B.1), $\pi_{\varepsilon,\tau}^*$ solves the balanced problem (EGW) between $\tilde{\mu}$ and $\tilde{\nu}$ with $\varepsilon' = m(\pi_{\varepsilon,\tau}^*) \varepsilon$, where $m(\pi_{\varepsilon,\tau}^*) = \pi_{\varepsilon,\tau}^*(\mathcal{X} \times \mathcal{Y})$ is the total mass of $\pi_{\varepsilon,\tau}^*$.

Definition B.1. A kernel $k : \mathbb{R}^d \times \mathbb{R}^d \rightarrow \mathbb{R}$ is conditionally positive (resp. negative) if it is symmetric and for any $\mathbf{x}_1, \dots, \mathbf{x}_n \in \mathbb{R}^d$ and $\mathbf{a} \in \mathbb{R}^n$ s.t. $\mathbf{a}^\top \mathbf{1}_n = 0$, one has

$$\sum_{i,j=1}^n a_i a_j k(\mathbf{x}_i, \mathbf{x}_j) \geq 0 \quad (\text{resp. } \leq 0)$$

Proof of 3.2. Step 1: Re-weightings. We first show that for $\pi_{\varepsilon,\tau}^*$ solution of EK problem, it exists $\eta, \xi : \mathbb{R}^d \rightarrow \mathbb{R}^+$ s.t. $\tilde{\mu} = p_1 \# \pi_{\varepsilon,\tau}^* = \eta \cdot \mu$ and $\tilde{\nu} = p_2 \# \pi_{\varepsilon,\tau}^* = \xi \cdot \nu$. We then remind the EK problem between μ and ν :

$$\min_{\pi \in \mathcal{M}^+(\mathcal{X} \times \mathcal{Y})} \int_{\mathcal{X} \times \mathcal{Y}} c(\mathbf{x}, \mathbf{y}) d\pi(\mathbf{x}, \mathbf{y}) + \varepsilon \text{KL}(\pi|\mu \otimes \nu) + \tau_1 \text{KL}(\pi_1|\mu) + \tau_2 \text{KL}(\pi_2|\nu). \quad (9)$$

The relative entropy term $\text{KL}(\pi|\mu \otimes \nu)$ in (9) is finite if and only if π admits a density with respect to $\mu \otimes \nu$. Therefore, one can reformulate 9 by restricting to the plan $\pi = h \cdot \mu \otimes \nu$ with (non-negative) relative density $h \in L_1^+(\mathcal{X} \times \mathcal{Y})$ w.r.t. $\mu \otimes \nu$. Moreover, in that case, the left marginal π_1 of π has a density h_1 w.r.t. μ and the right marginal π_2 has a density h_2 w.r.t. ν , and these densities are given by: $h_1(\cdot) := \int_{\mathcal{Y}} h(\cdot, \mathbf{y}) d\nu(\mathbf{y})$ and $h_2(\cdot) := \int_{\mathcal{X}} h(\mathbf{x}, \cdot) d\mu(\mathbf{x})$. Indeed, for any Borel set $A \subset \mathcal{X}$, one has:

$$\begin{aligned} \pi_1(A) &= \pi(A \times \mathcal{Y}) \\ &= \int_{\mathcal{X} \times \mathcal{Y}} 1_A(\mathbf{x}) f(\mathbf{x}, \mathbf{y}) d\mu(\mathbf{x}) d\nu(\mathbf{y}) \\ &= \int_{\mathcal{X}} 1_A(\mathbf{x}) \left(\int_{\mathcal{Y}} f(\mathbf{x}, \mathbf{y}) d\nu(\mathbf{y}) \right) d\mu(\mathbf{x}) \\ &= \int_{\mathcal{X}} 1_A(\mathbf{x}) h_1(\mathbf{x}) d\mu(\mathbf{x}) \end{aligned} \quad (10)$$

where the penultimate line follows from Fubini's theorem, so $\pi_1 = h_1 \cdot \mu$. We show similarly that $\pi_2 = h_2 \cdot \nu$. Therefore, one can reformulate (9) as:

$$\min_{h \in L_1^+(\mathcal{X} \times \mathcal{Y})} \int_{\mathcal{X} \times \mathcal{Y}} c(\mathbf{x}, \mathbf{y}) h(\mathbf{x}, \mathbf{y}) d\mu(\mathbf{x}) d\nu(\mathbf{y}) + \varepsilon \text{KL}(h|\mu \otimes \nu) + \tau_1 \text{KL}(h_1|\mu) + \tau_2 \text{KL}(h_2|\nu) \quad (11)$$

where we extend the KL divergence for densities: $\text{KL}(r|\gamma) = \int (r \log(r) + r - 1) d\gamma$. As a result, it exists $h^* \in L_1^+(\mathcal{X} \times \mathcal{Y})$ s.t. $\pi_{\varepsilon, \tau}^* = h^* \cdot \mu \otimes \nu$ and then $\tilde{\mu} = \eta \cdot \mu$ and $\tilde{\nu} = \xi \cdot \nu$ with $\eta = h_1^*$ and $\xi = h_2^*$. Moreover, by definition, $\pi_{\varepsilon, \tau}^*$ is a coupling between its marginal $\tilde{\mu}$ and $\tilde{\nu}$, so they have the same total mass. Indeed, using Fubini's Theorem twice, we get:

$$\int_{\mathcal{X} \times \mathcal{Y}} d\pi_{\varepsilon, \tau}^*(\mathbf{x}, \mathbf{y}) = \int_{\mathcal{X}} d\tilde{\mu}(\mathbf{x}) = \int_{\mathcal{Y}} d\tilde{\nu}(\mathbf{y}) \quad (12)$$

We now handle the Gromov-Wasserstein case, when $\pi_{\varepsilon, \tau}^*$ solve problem UEGW. We then remind problem UEGW between μ and ν :

$$\begin{aligned} \min_{\pi \in \mathcal{M}^+(\mathcal{X} \times \mathcal{Y})} \int_{(\mathcal{X} \times \mathcal{Y})^2} |c_{\mathcal{X}}(\mathbf{x}, \mathbf{x}') - c_{\mathcal{Y}}(\mathbf{y}, \mathbf{y}')|^2 d\pi(\mathbf{x}, \mathbf{y}) d\pi(\mathbf{x}', \mathbf{y}') \\ + \varepsilon \text{KL}^{\otimes}(\pi|\mu \otimes \nu) + \lambda_1 \text{KL}^{\otimes}(\pi_1|\mu) + \lambda_2 \text{KL}^{\otimes}(\pi_2|\nu), \end{aligned} \quad (13)$$

The relative entropy penalty is now quadratic: $\text{KL}^{\otimes}(\pi|\mu \otimes \nu) = \text{KL}(\pi \otimes \pi | (\mu \otimes \nu)^2)$, where $(\mu \otimes \nu)^2 = (\mu \otimes \nu) \otimes (\mu \otimes \nu)$ to lighten notations. Therefore, the above objective function is finite i.f.f. $\pi \otimes \pi$ has a density w.r.t. $(\mu \otimes \nu)^2$. Using arguments similar to the ones used above, it means that the marginals of $\pi \otimes \pi$ have a density w.r.t. the marginals of $(\mu \otimes \nu)^2$, which implies that π has a density w.r.t. $(\mu \otimes \nu)$. Now, we get the result by following exactly the same strategy as above.

Remark B.2. Note that in both cases, since $d\tilde{\mu}(\mathbf{x}) = \eta(\mathbf{x}) d\mu(\mathbf{x})$ and $d\tilde{\nu}(\mathbf{y}) = \xi(\mathbf{y}) d\nu(\mathbf{y})$, the equality of mass of $\tilde{\mu}$ and $\tilde{\nu}$ yields $\mathbb{E}_{X \sim \mu}[\eta(X)] = \mathbb{E}_{Y \sim \nu}[\xi(Y)]$.

Step 2: Optimality in the balanced problem for the Kantorovich case. We now prove **point 1**, stating that if $\pi_{\varepsilon, \tau}^*$ solves problem UEK between μ and ν , then it solves problem EK between $\tilde{\mu}$ and $\tilde{\nu}$ for the same entropic regularization strength ε .

We rely on duality and the specific structure of the optimal density h^* s.t. $\pi_{\varepsilon, \tau}^* = h^* \cdot \mu \otimes \nu$. Thanks to Séjourné et al. (2023a, Prop. 2), one has the existence of the so-called entropic potentials $f^* \in \mathcal{C}(\mathcal{X})$, $g^* \in \mathcal{C}(\mathcal{Y})$ s.t.

$$h^*(\mathbf{x}, \mathbf{y}) = \frac{d\pi_{\varepsilon, \tau}^*}{d(\mu \otimes \nu)}(\mathbf{x}, \mathbf{y}) = \exp\left(\frac{f^*(\mathbf{x}) + g^*(\mathbf{y}) - c(\mathbf{x}, \mathbf{y})}{\varepsilon}\right) \quad (14)$$

Moreover, by Nutz, Theorem 4.2, such a decomposition is equivalent to the optimality in problem EK. Therefore, $\pi_{\varepsilon, \tau}^*$ is solves problem EK between its marginals $\tilde{\mu}$ and $\tilde{\nu}$, i.e.

$$\pi_{\varepsilon, \tau}^* = \arg \min_{\pi \in \Pi(\tilde{\mu}, \tilde{\nu})} \int_{\mathcal{X} \times \mathcal{Y}} c(\mathbf{x}, \mathbf{y}) d\pi(\mathbf{x}, \mathbf{y}) + \varepsilon \text{KL}(\pi|\mu \otimes \nu). \quad (15)$$

Step 3: Optimality in the balanced problem for the Gromov-Wasserstein case. We now prove **point 2**, stating that, provided that the costs $c_{\mathcal{X}}$ and $c_{\mathcal{Y}}$ are conditionally positive (or conditionally negative), if $\pi_{\varepsilon, \tau}^*$ is a solves problem UEGW between μ and ν , then it solves problem EGW between $\tilde{\mu}$ and $\tilde{\nu}$ for the entropic regularization strength $\varepsilon' = m(\pi_{\varepsilon, \tau}^*) \varepsilon$.

Define the functional:

$$\begin{aligned} F : (\gamma, \pi) \in \mathcal{M}^+(\mathcal{X} \times \mathcal{Y})^2 \mapsto \int_{(\mathcal{X} \times \mathcal{Y})^2} |c_{\mathcal{X}}(\mathbf{x}, \mathbf{x}') - c_{\mathcal{Y}}(\mathbf{y}, \mathbf{y}')|^2 d\pi(\mathbf{x}, \mathbf{y}) d\gamma(\mathbf{x}', \mathbf{y}') \\ + \varepsilon \text{KL}(\pi \otimes \gamma | (\mu \otimes \nu)^2) + \lambda_1 \text{KL}(\pi_1 \otimes \gamma_1 | \mu \times \mu) + \lambda_2 \text{KL}^{\otimes}(\pi_2 \otimes \gamma_2 | \nu \times \nu), \end{aligned} \quad (16)$$

s.t. $\pi_{\varepsilon, \tau}^* \in \arg \min_{\pi \in \mathcal{M}(\mathcal{X} \times \mathcal{Y})} F(\pi, \pi)$. By first-order condition, one has:

$$\pi_{\varepsilon, \tau}^* \in \arg \min_{\gamma \in \mathcal{M}(\mathcal{X} \times \mathcal{Y})} F(\gamma, \pi_{\varepsilon, \tau}^*) \quad (17)$$

We then define the linearized cost

$$c_{\varepsilon,\tau}^* : (\mathbf{x}, \mathbf{y}) \in \mathcal{X} \times \mathcal{Y} \mapsto \int_{\mathcal{X} \times \mathcal{Y}} |c_{\mathcal{X}}(\mathbf{x}, \mathbf{x}') - c_{\mathcal{Y}}(\mathbf{y}, \mathbf{y}')|^2 d\pi_{\varepsilon,\tau}^*(\mathbf{x}', \mathbf{y}'), \quad (18)$$

s.t. from (Séjourné et al., 2023a)[Proposition 9], (18) implies that $\pi_{\varepsilon,\tau}^*$ solves:

$$\begin{aligned} \pi_{\varepsilon,\tau}^* \in \arg \min_{\pi \in \mathcal{M}(\mathcal{X} \times \mathcal{Y})} & \int_{\mathcal{X} \times \mathcal{Y}} c_{\varepsilon,\tau}^*(\mathbf{x}, \mathbf{y}) d\pi(\mathbf{x}, \mathbf{y}) + \varepsilon m(\pi_{\varepsilon,\tau}^*) \text{KL}(\pi | \mu \otimes \nu) \\ & + \lambda_1 m(\pi_{\varepsilon,\tau}^*) \text{KL}(\pi_1 | \mu) + \lambda_2 m(\pi_{\varepsilon,\tau}^*) \text{KL}(\pi_2 | \nu). \end{aligned} \quad (19)$$

so $\pi_{\varepsilon,\tau}^*$ solves problem UEK between μ and ν for a new cost $c_{\varepsilon,\tau}^*$, and the regularization strength $\varepsilon' = \varepsilon m(\pi_{\varepsilon,\tau}^*)$. We seek to apply point 1, to get that $\pi_{\varepsilon,\tau}^*$ solves problem EK between $\tilde{\mu} = p_1 \# \pi_{\varepsilon,\tau}^*$ and $\tilde{\nu} = p_2 \# \pi_{\varepsilon,\tau}^*$ for the same entropic regularization strength ε' . To that end, we first verify that $c_{\varepsilon,\tau}^*$ is continuous. For every $\mathbf{x}, \mathbf{x}' \in \mathcal{X}$ and $\mathbf{y}, \mathbf{y}' \in \mathcal{Y}$, one has

$$\begin{aligned} |c_{\mathcal{X}}(\mathbf{x}, \mathbf{x}') - c_{\mathcal{Y}}(\mathbf{y}, \mathbf{y}')|^2 & \leq |c_{\mathcal{X}}(\mathbf{x}, \mathbf{x}')|^2 + |c_{\mathcal{Y}}(\mathbf{y}, \mathbf{y}')|^2 \\ & \leq \sup_{\mathbf{x}, \mathbf{x}' \in \mathcal{X}} |c_{\mathcal{X}}(\mathbf{x}, \mathbf{x}')|^2 + \sup_{\mathbf{y}, \mathbf{y}' \in \mathcal{Y}} |c_{\mathcal{Y}}(\mathbf{y}, \mathbf{y}')|^2 \\ & < +\infty \end{aligned} \quad (20)$$

where the last line follows from the fact that $c_{\mathcal{X}}$ and $c_{\mathcal{Y}}$ are continuous on $\mathcal{X} \times \mathcal{X}$ and $\mathcal{Y} \times \mathcal{Y}$, which are compact sets as product of compact sets. Then, since $\pi_{\varepsilon,\tau}^*$ has finite mass, Lebesgue's dominated convergence yields the continuity of $c_{\varepsilon,\tau}^*$. We then to apply point 1 and get:

$$\pi_{\varepsilon,\tau}^* \in \arg \min_{\pi \in \Pi(\tilde{\mu}, \tilde{\nu})} \int_{\mathcal{X} \times \mathcal{Y}} c_{\varepsilon,\tau}^*(\mathbf{x}, \mathbf{y}) d\pi(\mathbf{x}, \mathbf{y}) + \varepsilon' \text{KL}(\pi | \mu \otimes \nu) \quad (21)$$

Since the costs are conditionally positive (or conditionally negative) kernels, (21) finally yields the desired result by applying (Séjourné et al., 2023b)[Theorem 3]:

$$\pi_{\varepsilon,\tau}^* \in \arg \min_{\pi \in \Pi(\tilde{\mu}, \tilde{\nu})} \int_{\mathcal{X} \times \mathcal{Y}} |c_{\mathcal{X}}(\mathbf{x}, \mathbf{x}') - c_{\mathcal{Y}}(\mathbf{y}, \mathbf{y}')| d\pi(\mathbf{x}', \mathbf{y}') d\pi(\mathbf{x}, \mathbf{y}) + \varepsilon' \text{KL}(\pi | \mu \otimes \nu) \quad (22)$$

□

Proposition 3.3 (Estimation of the re-weightings.). *Let $\hat{\pi}_{\varepsilon,\tau}$ the solution of (UEK) computed on samples. Let $\mathbf{a} = \hat{\pi}_{\varepsilon,\tau} \mathbf{1}_n$ and $\mathbf{b} = \hat{\pi}_{\varepsilon,\tau}^\top \mathbf{1}_n$ be its marginal weights and let $\hat{\eta}_n(\mathbf{x}_i) := n a_i$ and $\hat{\xi}_n(\mathbf{y}_i) := n b_i$. Then, almost surely, $\hat{\eta}_n(\mathbf{x}_i) \rightarrow \eta(\mathbf{x}_i)$ and $\hat{\xi}_n(\mathbf{y}_i) \rightarrow \xi(\mathbf{y}_i)$.*

Proof. We remind that we here consider π_{ε}^* the solution of problem EK between μ and ν , and $\tilde{\mu} = \eta \cdot \mu$ and $\tilde{\nu} = \xi \cdot \nu$ denote its marginals. As we saw in the proof of Prop.3.2, using Séjourné et al. (2023a, Prop. 2), one has the existence of $f^* \in C(\mathcal{X})$ and $g^* \in C(\mathcal{Y})$ s.t.

$$\frac{d\pi_{\varepsilon}^*}{d(\mu \otimes \nu)}(\mathbf{x}, \mathbf{y}) = \exp \left(\frac{f^*(\mathbf{x}) + g^*(\mathbf{y}) - c(\mathbf{x}, \mathbf{y})}{\varepsilon} \right)$$

Therefore, the relative densities are

$$\begin{aligned} \eta : \mathbf{x} & \mapsto \int_{\mathcal{Y}} \exp \left(\frac{f^*(\mathbf{x}) + g^*(\mathbf{y}) - c(\mathbf{x}, \mathbf{y})}{\varepsilon} \right) d\nu(\mathbf{y}) \\ \xi : \mathbf{y} & \mapsto \int_{\mathcal{X}} \exp \left(\frac{f^*(\mathbf{x}) + g^*(\mathbf{y}) - c(\mathbf{x}, \mathbf{y})}{\varepsilon} \right) d\mu(\mathbf{x}) \end{aligned} \quad (23)$$

□

Now, let consider $\hat{\pi}_{\varepsilon,\tau}$ the solution of problem EK between $\hat{\mu}_n$ and $\hat{\nu}_n$. Still applying Séjourné et al. (2023a, Prop. 2), one has the existence of $f_n^* \in C(\mathcal{X})$ and $g_n^* \in C(\mathcal{Y})$ s.t.

$$\frac{d\hat{\pi}_{\varepsilon,\tau}}{d(\hat{\mu}_n \otimes \hat{\nu}_n)}(\mathbf{x}, \mathbf{y}) = \exp \left(\frac{f_n^*(\mathbf{x}) + g_n^*(\mathbf{y}) - c(\mathbf{x}, \mathbf{y})}{\varepsilon} \right) \quad (24)$$

Writing $\hat{\pi}_{\varepsilon, \tau} = \sum_{i,j=1}^n \hat{\pi}_{\varepsilon, \tau}^{ij} \delta_{(\mathbf{x}_i, \mathbf{y}_j)}$, (24) implies that

$$\hat{\pi}_{\varepsilon, \tau}^{ij} = \frac{1}{n^2} \exp \left(\frac{f_n^*(\mathbf{x}_i) + g_n^*(\mathbf{y}_j) - c(\mathbf{x}_i, \mathbf{y}_j)}{\varepsilon} \right) \quad (25)$$

where the potentials f_n^* , g_n^* now appear from their values on the samples \mathbf{x}_i , \mathbf{y}_j . Reminding that $\mathbf{a} = \hat{\pi}_{\varepsilon, \tau} \mathbf{1}_n$ and $\mathbf{b} = \hat{\pi}_{\varepsilon, \tau}^\top \mathbf{1}_n$ and combining that with (25), one has:

$$\begin{aligned} n a_i &= \frac{1}{n} \sum_{j=1}^n \exp \left(\frac{f_n^*(\mathbf{x}_i) + g_n^*(\mathbf{y}_j) - c(\mathbf{x}_i, \mathbf{y}_j)}{\varepsilon} \right) \\ n b_i &= \frac{1}{n} \sum_{j=1}^n \exp \left(\frac{f_n^*(\mathbf{x}_i) + g_n^*(\mathbf{y}_j) - c(\mathbf{x}_i, \mathbf{y}_j)}{\varepsilon} \right) \end{aligned} \quad (26)$$

Almost surely, $\hat{\mu}_n \rightarrow \mu$ and $\hat{\nu}_n \rightarrow \nu$, so using (Séjourné et al., 2021)[Proposition 10], $f_n^* \rightarrow f^*$ and $g_n^* \rightarrow g^*$ in sup-norm. Then, define:

$$\begin{aligned} \hat{\eta}_n : \mathbf{x} &\mapsto \frac{1}{n} \sum_{j=1}^n \exp \left(\frac{f_n^*(\mathbf{x}) + g_n^*(\mathbf{y}_j) - c(\mathbf{x}, \mathbf{y}_j)}{\varepsilon} \right) \\ \hat{\xi}_n : \mathbf{y} &\mapsto \frac{1}{n} \sum_{j=1}^n \exp \left(\frac{f_n^*(\mathbf{x}_i) + g_n^*(\mathbf{y}) - c(\mathbf{x}_i, \mathbf{y})}{\varepsilon} \right) \end{aligned} \quad (27)$$

s.t. $\hat{\eta}_n(\mathbf{x}_i) = n a_i$ and $\hat{\xi}_n(\mathbf{y}_i) = n b_i$. Instead of just showing the convergence in each of these points, we can even show that almost surely, $\hat{\eta}_n \rightarrow \eta$ and $\hat{\xi}_n \rightarrow \xi$ pointwise. Let us show this result for $\hat{\eta}_n$. First, we define:

$$\begin{aligned} h_n : (\mathbf{x}, \mathbf{y}) &\mapsto \exp \left(\frac{f_n^*(\mathbf{x}) + g_n^*(\mathbf{y}) - c(\mathbf{x}, \mathbf{y})}{\varepsilon} \right) \\ h : (\mathbf{x}, \mathbf{y}) &\mapsto \exp \left(\frac{f^*(\mathbf{x}) + g^*(\mathbf{y}) - c(\mathbf{x}, \mathbf{y})}{\varepsilon} \right) \end{aligned} \quad (28)$$

such that $\hat{\eta}_n : \mathbf{x} \mapsto \int_{\mathcal{Y}} h_n(\mathbf{x}, \mathbf{y}) d\hat{\nu}_n(\mathbf{y})$ and $\eta : \mathbf{x} \mapsto \int_{\mathcal{Y}} h(\mathbf{x}, \mathbf{y}) d\nu(\mathbf{y})$

Since $f_n^* \rightarrow f^*$ on \mathcal{X} and $g_n^* \rightarrow g^*$ on \mathcal{Y} in sup-norm, $h_n \rightarrow h$ in sup-norm on $\mathcal{X} \times \mathcal{Y}$. Indeed, for $(\mathbf{x}, \mathbf{y}) \in (\mathcal{X} \times \mathcal{Y})$, one has:

$$\begin{aligned} &|h_n(\mathbf{x}, \mathbf{y}) - h(\mathbf{x}, \mathbf{y})| \\ &= \left| \exp \left(\frac{f_n^*(\mathbf{x}) + g_n^*(\mathbf{y}) - c(\mathbf{x}, \mathbf{y})}{\varepsilon} \right) - \exp \left(\frac{f^*(\mathbf{x}) + g^*(\mathbf{y}) - c(\mathbf{x}, \mathbf{y})}{\varepsilon} \right) \right| \\ &= \exp \left(\frac{c(\mathbf{x}, \mathbf{y})}{\varepsilon} \right) \left| \exp \left(\frac{f_n^*(\mathbf{x}) + g_n^*(\mathbf{y})}{\varepsilon} \right) - \exp \left(\frac{f^*(\mathbf{x}) + g^*(\mathbf{y})}{\varepsilon} \right) \right| \\ &\leq M_{c, \varepsilon} \left| \exp \left(\frac{f_n^*(\mathbf{x}) + g_n^*(\mathbf{y})}{\varepsilon} \right) - \exp \left(\frac{f^*(\mathbf{x}) + g^*(\mathbf{y})}{\varepsilon} \right) \right| \end{aligned} \quad (29)$$

with $M_{c, \varepsilon} = \sup_{(\mathbf{x}, \mathbf{y}) \in \mathcal{X} \times \mathcal{Y}} \exp \left(\frac{c(\mathbf{x}, \mathbf{y})}{\varepsilon} \right) < +\infty$, since the cost is continuous on the compact $\mathcal{X} \times \mathcal{Y}$, so is $(\mathbf{x}, \mathbf{y}) \mapsto \exp \left(\frac{c(\mathbf{x}, \mathbf{y})}{\varepsilon} \right)$. Then,

$$\begin{aligned} &\left| \exp \left(\frac{f_n^*(\mathbf{x}) + g_n^*(\mathbf{y})}{\varepsilon} \right) - \exp \left(\frac{f^*(\mathbf{x}) + g^*(\mathbf{y})}{\varepsilon} \right) \right| \\ &\leq \left| \exp \left(\frac{f_n^*(\mathbf{x})}{\varepsilon} \right) \exp \left(\frac{g_n^*(\mathbf{y})}{\varepsilon} \right) - \exp \left(\frac{f_n^*(\mathbf{x})}{\varepsilon} \right) \exp \left(\frac{g^*(\mathbf{y})}{\varepsilon} \right) \right| \\ &\quad + \left| \exp \left(\frac{f_n^*(\mathbf{x})}{\varepsilon} \right) \exp \left(\frac{g^*(\mathbf{y})}{\varepsilon} \right) - \exp \left(\frac{f^*(\mathbf{x})}{\varepsilon} \right) \exp \left(\frac{g^*(\mathbf{y})}{\varepsilon} \right) \right| \end{aligned} \quad (30)$$

For the first term, one has:

$$\begin{aligned}
& \left| \exp\left(\frac{f_n^*(\mathbf{x})}{\varepsilon}\right) \exp\left(\frac{g_n^*(\mathbf{x})}{\varepsilon}\right) - \exp\left(\frac{f_n^*(\mathbf{x})}{\varepsilon}\right) \exp\left(\frac{g^*(\mathbf{x})}{\varepsilon}\right) \right| \\
&= \exp\left(\frac{f_n^*(\mathbf{x})}{\varepsilon}\right) \left| \exp\left(\frac{g_n^*(\mathbf{x})}{\varepsilon}\right) - \exp\left(\frac{g^*(\mathbf{x})}{\varepsilon}\right) \right| \\
&\leq \exp\left(\frac{\|f_n^*\|_\infty}{\varepsilon}\right) \left| \exp\left(\frac{g_n^*(\mathbf{x})}{\varepsilon}\right) - \exp\left(\frac{g^*(\mathbf{x})}{\varepsilon}\right) \right|
\end{aligned} \tag{31}$$

First, we can bound uniformly $\exp(\|f_n^*\|_\infty/\varepsilon)$ since f_n converges in sup-norm, so $(\|f_n^*\|_\infty)_{n \geq 0}$ is bounded. Then, since g_n^* converges in sup-norm, it is uniformly bounded, and since g^* is continuous on the compact \mathcal{X} , it is bounded. Therefore, we can find a compact $K \subset \mathbb{R}$ s.t. $g^*(\mathcal{X}) \subset K$ and for each n , $g_n^*(\mathcal{X}) \subset K$. Then, applying the mean value theorem to the C_1 function $\mathbf{x} \mapsto \exp(\mathbf{x}/\varepsilon)$ on K , we can bound:

$$\left| \exp\left(\frac{g_n^*(\mathbf{x})}{\varepsilon}\right) - \exp\left(\frac{g^*(\mathbf{x})}{\varepsilon}\right) \right| \leq \sup_{\mathbf{z} \in K} \frac{1}{\varepsilon} \exp\left(\frac{1}{\varepsilon} \mathbf{z}\right) |g_n^*(\mathbf{x}) - g^*(\mathbf{x})| \tag{32}$$

Finally, this yields the existence of a constant $M_1 > 0$ s.t.

$$\left| \exp\left(\frac{f_n^*(\mathbf{x})}{\varepsilon}\right) \exp\left(\frac{g_n^*(\mathbf{x})}{\varepsilon}\right) - \exp\left(\frac{f_n^*(\mathbf{x})}{\varepsilon}\right) \exp\left(\frac{g^*(\mathbf{x})}{\varepsilon}\right) \right| \leq M_1 \|g_n^* - g^*\|_\infty \tag{33}$$

Using the same strategy, we get the existence of a constant $M_2 > 0$ s.t.

$$\left| \exp\left(\frac{f_n^*(\mathbf{x})}{\varepsilon}\right) \exp\left(\frac{g^*(\mathbf{x})}{\varepsilon}\right) - \exp\left(\frac{f^*(\mathbf{x})}{\varepsilon}\right) \exp\left(\frac{g^*(\mathbf{x})}{\varepsilon}\right) \right| \leq M_2 \|f_n^* - f^*\|_\infty \tag{34}$$

Combining (33) and (34) with (B.1) and (29), we get that:

$$|h_n(\mathbf{x}) - h(\mathbf{x})| \leq M_{c,\varepsilon} (M_1 \|g_n^* - g^*\|_\infty + M_2 \|f_n^* - f^*\|_\infty) \tag{35}$$

from which we can deduce that $h_n \rightarrow h$ in sup-norm, from the convergence of $f_n \rightarrow f$ and $g_n \rightarrow g$ in sup-norm.

Now, we can show the pointwise convergence of $\hat{\eta}_n$. For any $\mathbf{x} \in \mathcal{X}$, one has:

$$\begin{aligned}
& |\hat{\eta}_n(\mathbf{x}) - \eta(\mathbf{x})| \\
&= \left| \int h_n(\mathbf{x}, \mathbf{y}) d\hat{\nu}_n(\mathbf{y}) - \int h(\mathbf{x}, \mathbf{y}) d\nu(\mathbf{y}) \right| \\
&\leq \left| \int h_n(\mathbf{x}, \mathbf{y}) d\hat{\nu}_n(\mathbf{y}) - \int h(\mathbf{x}, \mathbf{y}) d\hat{\nu}_n(\mathbf{y}) \right| + \left| \int h(\mathbf{x}, \mathbf{y}) d\hat{\nu}_n(\mathbf{y}) - \int h(\mathbf{x}, \mathbf{y}) d\nu(\mathbf{y}) \right| \\
&\leq \int \|h_n - h\|_\infty d\hat{\nu}_n(\mathbf{y}) + \left| \int h(\mathbf{x}, \mathbf{y}) d\hat{\nu}_n(\mathbf{y}) - \int h(\mathbf{x}, \mathbf{y}) d\nu(\mathbf{y}) \right| \\
&= \|h_n - h\|_\infty + \left| \int h(\mathbf{x}, \mathbf{y}) d\hat{\nu}_n(\mathbf{y}) - \int h(\mathbf{x}, \mathbf{y}) d\nu(\mathbf{y}) \right|
\end{aligned} \tag{36}$$

Therefore, it almost surely holds that $\hat{\eta}_n(\mathbf{x}) \rightarrow \eta(\mathbf{x})$. Indeed, $\|h_n - h\|_\infty \rightarrow 0$ since we have shown that $h_n \rightarrow h$ in sup-norm. Then, h is continuous on the compact $\mathcal{X} \times \mathcal{Y}$, so it is bounded, so since $\mu_n \rightarrow \mu$, we get $\int h d\hat{\nu}_n \rightarrow \int h d\nu$. Next, we show similarly that, almost surely, $\hat{\xi}_n \rightarrow \xi$ pointwise. This finally yields that $\hat{\eta}_n(\mathbf{x}_i) \rightarrow \eta(\mathbf{x}_i)$ and $\hat{\xi}_n(\mathbf{x}_i) \rightarrow \xi(\mathbf{y}_i)$

C METRICS

We start with introducing general metrics in § C.1, some of which will be used in the metrics introduced in the context of experiments on single-cell data in § C.2.

C.1 GENERAL METRICS

In the following, we discuss a way how to classify predictions in a generative model. We start with the setting where each mapped sample is to be assigned to a category based on labelled data in the target distribution. We then continue with the case where there are also labels for samples in the source distribution, and this way define a classifier f_{class} between labels in the source distribution and labels in the target distribution. Building upon this, we assign the classifier f_{class} an uncertainty score for each prediction. Finally, we define a calibration score assessing the quality of a given uncertainty score.

Turning a generative model into a classifier In the following, consider a finite set of samples in the target domain $\mathbf{y}_1, \dots, \mathbf{y}_M \in \mathcal{Y}$. Assume $\{\mathbf{y}_m\}_{m=1}^M$ allows for a partition $\{\mathbf{y}_m\}_{m=1}^M = \sqcup_{k \in K} \mathcal{T}_k$. Hence, each sample belongs to exactly one class, which we interchangeably refer to as the sample being labelled. Let $T : \mathcal{X} \rightarrow \mathcal{Y}$ be a map (deterministic or stochastic), and let $f_{1\text{-NN}} : \mathcal{Y} \rightarrow \{\mathcal{T}_k\}_{k=1}^K$ be the 1-nearest neighbor classifier. We obtain a map g from \mathcal{X} to $\{\mathcal{T}_k\}_{k=1}^K \subset \mathcal{Y}$ by the concatenation of $f_{1\text{-NN}}$ and T . This map g proves useful in settings when mapped cells are to be categorized, e.g. to assign mapped cells to a cell type.

A metric to assess the accuracy of a generative model In the following, assume that the set of samples in the source domain $\mathbf{x}_1, \dots, \mathbf{x}_N$ allows for a partition $\{\mathbf{x}_n\}_{n=1}^N = \sqcup_{k \in K} \mathcal{S}_k$. Note that the number of elements in the partition of both the source and the target domain is set to K . We want to construct a classifier f_{class} assigning each category in the source distribution $\{\mathcal{S}_k\}_{k=1}^K$ probabilistically to a category in the target distribution $\{\mathcal{T}_k\}_{k=1}^K$. Define $f_{\text{class}} : \{\mathcal{S}_k\}_{k=1}^K \rightarrow \mathbb{N}^K$ via $(f_{\text{class}}(\mathcal{S}_k))_j = \sum_{\mathbf{x}_n \in \mathcal{S}_k} 1_{\{g(\mathbf{x}_n) = \mathcal{T}_j\}}$ where $g : \mathcal{X} \rightarrow \{\mathcal{T}_k\}_{k=1}^K$ was defined above.

Assume that there exists a known one-to-one match between elements in $\{\mathcal{S}_k\}_{k=1}^K$ and elements in $\{\mathcal{T}_k\}_{k=1}^K$. Then we can define a confusion matrix \mathcal{A} with entries $\mathcal{A}_{ij} := \sum_{\mathbf{x}_n \in \mathcal{T}_i} 1_{\{g(\mathbf{x}_n) = \mathcal{S}_j\}}$. In the context of entropic OT the confusion matrix is element-wise defined as

$$\mathcal{A}_{ij} := \sum_{\mathbf{x}_n \in \mathcal{T}_i} 1_{\{f_{1\text{-NN}}(T(\mathbf{x}_n)) = \mathcal{S}_j\}} \quad (37)$$

This way we obtain an accuracy score of the classifier f_{class} mapping a partition of one set of samples to a partition of another set of samples.

Calibration score To assess the meaningfulness of an uncertainty score, we introduce the following calibration score. Assume we have a classifier which yields predictions along with uncertainty estimations. Let $\mathbf{u} \in \mathbb{R}^K$ be a vector containing an uncertainty estimation for each element in $\{\mathcal{S}_k\}_{k=1}^K$. Moreover, let $\mathbf{a} \in \mathbb{R}^K$ be a vector containing the accuracy for each element in $\{\mathcal{S}_k\}_{k=1}^K$. We then define our calibration score to be the Spearman rank correlation coefficient between \mathbf{u} and $\mathbf{1}_K - \mathbf{a}$, where $\mathbf{1}_K$ denotes the K -dimensional vector containing 1 in every entry. In effect, the calibration score is close to 1 if the model assigns high uncertainty to wrong predictions and low uncertainty to true predictions, while the calibration score is close to -1 if the model assigns high uncertainty to correct predictions and low uncertainty to wrong predictions.

In the following, we consider a stochastic map T . Let $\mathbf{y}_1, \dots, \mathbf{y}_L \sim \hat{\pi}_\varepsilon(\cdot|\mathbf{x})$ obtained from T . To obtain a calibration score for f_{class} we estimate a statistic $V(\hat{\pi}_\varepsilon(\cdot|\mathbf{x}))$ from the samples $\mathbf{y}_1, \dots, \mathbf{y}_L$, reflecting an estimation of uncertainty. Then, we let the uncertainty of the prediction of f_{class} for category \mathcal{S}_i be the mean uncertainty statistic, i.e. $\sum_{\mathbf{x} \in \mathcal{S}_i} \frac{V(\hat{\pi}_\varepsilon(\cdot|\mathbf{x}))}{|\mathcal{S}_i|}$. In effect, for each prediction $f_{\text{class}}(\mathcal{S}_i)$ we get the uncertainty score

$$u_i = \sum_{\mathbf{x} \in \mathcal{S}_i} \frac{V(\hat{\pi}_\varepsilon(\cdot|\mathbf{x}))}{|\mathcal{S}_i|}. \quad (38)$$

Assessing the uncertainty with the *cos-var* metric Gayoso et al. (2022) introduce a statistic to assess the uncertainty of deep generative RNA velocity methods from samples of the posterior distribution, which we adapt to the OT paradigm to obtain

$$\text{cos-var}(\hat{\pi}_\varepsilon(\cdot|\mathbf{x})) = \text{Var}_{Y \sim \hat{\pi}_\varepsilon(\cdot|\mathbf{x})}[\text{cos-sim}(Y, \mathbb{E}_{Y \sim \hat{\pi}_\varepsilon(\cdot|\mathbf{x})}[Y])], \quad (39)$$

where cos-sim denotes the cosine similarity. We refer to this metric as cos-var, as it computes the variance of the cosine similarity of samples following the conditional distribution and the conditional mean. We use 30 samples from the conditional distribution to compute this metric.

C.2 SINGLE-CELL SPECIFIC METRICS

Cell type / cell lineage transition scores As in most single-cell tasks there is no ground truth of matches between cells, we rely on labels of clusters of the data, i.e. on cell types. We then assess the accuracy of a generative model by considering the accuracy of the corresponding classifier f_{class} as described above. The correct matches between classes have to be considered task-specifically. In the following, we discuss the choice of the labels $\{\mathcal{S}_k\}_{k=1}^K$ and $\{\mathcal{T}_k\}_{k=1}^K$ for different tasks.

- U-GENOT-K for pancreas development: Cells of the developing mouse pancreas (at the time points we consider, i.e. embryonic day 14.5, corresponding to the source distribution, and 15.5, corresponding to the target distribution) can be classified into two lineages (Bastidas-Ponce et al., 2019), which both originate from a *Multipotent* cell population. These lineages are the Acinar (A) lineage, and the ED lineage containing endocrine and ductal cells. Thus, we define $\{\mathcal{S}_k\}_{k=1}^K = \{\mathcal{T}_k\}_{k=1}^K = \{A, ED\}$ as we know that cells in the A lineage won't develop into cells belonging to the ED lineage, and vice versa.
- U-GENOT-K for perturbation prediction: Each drug was applied to cells belonging to three different cell types/cell lines, namely A549, K562, and MCF7. Hence, we can define $\{\mathcal{S}_k\}_{k=1}^K = \{\mathcal{T}_k\}_{k=1}^K = \{A549, K562, MCF7\}$ as for each perturbed cell we know the cell type at the time of injecting the drug.

FOSCTTM score In the following, we consider a setting where the true match between *samples* is known. The FOSCTTM score ("Fraction of Samples Closer than True Match") measures the fraction of cells which are closer to the true match than the predicted cell. Hence, a random match has a FOSCTTM score of 0.5, while a perfect match has a FOSCTTM score of 0.0. In the following we only consider discrete distributions. To define the FOSCTTM score for a map $T : \mathcal{X} \rightarrow \mathcal{Y}$, let $\mathbf{x}_1, \dots, \mathbf{x}_K \in \mathcal{X}$ be samples from the source distribution and $\mathbf{y}_1, \dots, \mathbf{y}_K \in \mathcal{Y}$ be samples from the target distribution, such that \mathbf{x}_k and \mathbf{y}_k form a true match. Moreover, let $\hat{\mathbf{y}}_k = T(\mathbf{x}_k)$. Let

$$p_j = \frac{\sum_{k \in K} \mathbf{1}_{\|\mathbf{y}_k - \hat{\mathbf{y}}_j\|_2^2 \leq \|\mathbf{y}_j - \hat{\mathbf{y}}_j\|_2^2}}{|K|} \quad (40)$$

and

$$q_j = \frac{\sum_{k \in K} \mathbf{1}_{\|\mathbf{y}_j - \hat{\mathbf{y}}_k\|_2^2 \leq \|\mathbf{y}_j - \hat{\mathbf{y}}_k\|_2^2}}{|K|} \quad (41)$$

Then, the FOSCTTM score between the predicted target $\{\hat{\mathbf{y}}_k\}_{k \in K}$ and the target $\{\mathbf{y}_k\}_{k \in K}$ is obtained as

$$\text{FOSCTMM}(\{\hat{\mathbf{y}}_k\}_{k \in K}, \{\mathbf{y}_k\}_{k \in K}) = \sum_{k \in K} \frac{p_j + q_j}{2}. \quad (42)$$

D DATASETS

D.1 PANCREAS SINGLE-CELL DATASET

The dataset of the developing mouse pancreas was published in Bastidas-Ponce et al. (2019) and can be downloaded following the guidelines on <https://www.ncbi.nlm.nih.gov/geo/query/acc.cgi?acc=GSE132188>. The full dataset contains measurements of embryonic days 12.5, 13.5, 14.5, and 15.5, while we only consider time points 14.5 and 15.5.

Benchmark & uncertainty evaluation For the benchmark against competing methods we filter the dataset such that we only keep cells belonging to the cell types of the endocrine branch to ensure that learnt transitions are biologically plausible. Moreover, cells annotated as *Ngn3 high cycling* were removed due to its unknown stage in the developmental process (Bastidas-Ponce et al., 2019). The removal is justified by the small number of cells belonging to this cell type and its outlying position in gene expression space. For the uncertainty analysis presented in 2 we use the same

dataset. The final list of cell types included can hence be found in figure 10. The benchmark was performed on 30-dimensional PCA space of log-transformed gene expression counts.

Application in the unbalanced case For demonstrating the capabilities of UGENOT-K, we use all cells belonging to E14.5 or E15.5 except for Multipotent cells as these cells can develop into either of the considered cell lineages ED or A, hence the cell type transition score as defined in appendix C.1 could not be computed.

D.2 DRUG PERTURBATION SINGLE-CELL DATASET

The dataset was published in (Srivatsan et al., 2020). We download the dataset following the instructions detailed on <https://github.com/bunnech/cellot/tree/main>.

For all analyses (figure 3) we computed PCA embeddings on the filtered dataset including the control cells and the corresponding drug only. This ensures the capturing of relevant distributional shifts and hence prevents the model from near-constant predictions as the effect of numerous drugs is weak.

D.3 HUMAN BONE MARROW SINGLE-CELL DATASET FOR MODALITY TRANSLATION

This dataset contains paired measurements of single-cell RNA-seq readouts and single-nucleus ATAC-seq measurements (Luecken et al., 2021). This means that we have a ground truth one-to-one matching for each cell. We use the processed data provided in moscot (Klein et al., 2023), which can be downloaded following the instructions on https://moscot.readthedocs.io/en/latest/genapi/moscot.datasets.bone_marrow.html#moscot.datasets.bone_marrow. This version of the dataset additionally contains a shared embedding for both the RNA and the ATAC data, which we use in the fused term. This embedding was created using a variational autoencoder (scVI (Lopez et al., 2018b)) by integrating the RNA counts of the gene expression dataset and gene activity (Stuart et al., 2021) derived from the ATAC data, a commonly used approximation for gene expression estimation from ATAC data (Heumos et al., 2023).

In RNA space we use the PCA embedding (the dimension of which is detailed in the corresponding experiments), while the embedding used in ATAC space is the given LSI (latent semantic indexing) embedding, followed by a feature-wise L2-normalization as proposed in Demetci et al. (2022).

E ADDITIONAL INFORMATION AND RESULTS FOR EXPERIMENTS

If not stated otherwise, the GENOT model configuration follows the setup described in appendix G.

E.1 1D SIMULATED DATA

While figure 1 shows results for $\tau = \tau_1 = \tau_2 = 0.98$, figure 7 visualizes the influence of τ . While $\tau = 1.0$ corresponds to the fully balanced case, setting $\tau = 0.97$ results in a complete discardment of one mode in the target distribution. The ground truth is computed with a discrete entropy-regularized OT solver (Cuturi et al., 2022).

E.2 GENOT-K

GENOT-K benchmark on the developing mouse pancreas dataset The benchmark is performed on the dataset capturing the development of the mouse pancreas (appendix D.1) by transporting cells from the early time point to the later time point. For the benchmark the data was standard-normalized to prevent performance issues of models which are not built for data ranges attained by PCA space of the processed single-cell RNA-seq data. The dataset was randomly divided into a 60/40 split of training and test set. As there is no ground truth match between cells in the source and the target distribution, we assess the performance of each model by measuring the Sinkhorn divergence (Feydy et al., 2019b) with regularization parameter $\varepsilon = 1e - 3$ between the test target dataset and the predicted test target dataset, i.e. the pushforward of the test source dataset. GENOT-K was run as described in appendix G, but iterations were increased to 20_000. Details on competing methods can be found in appendix F.

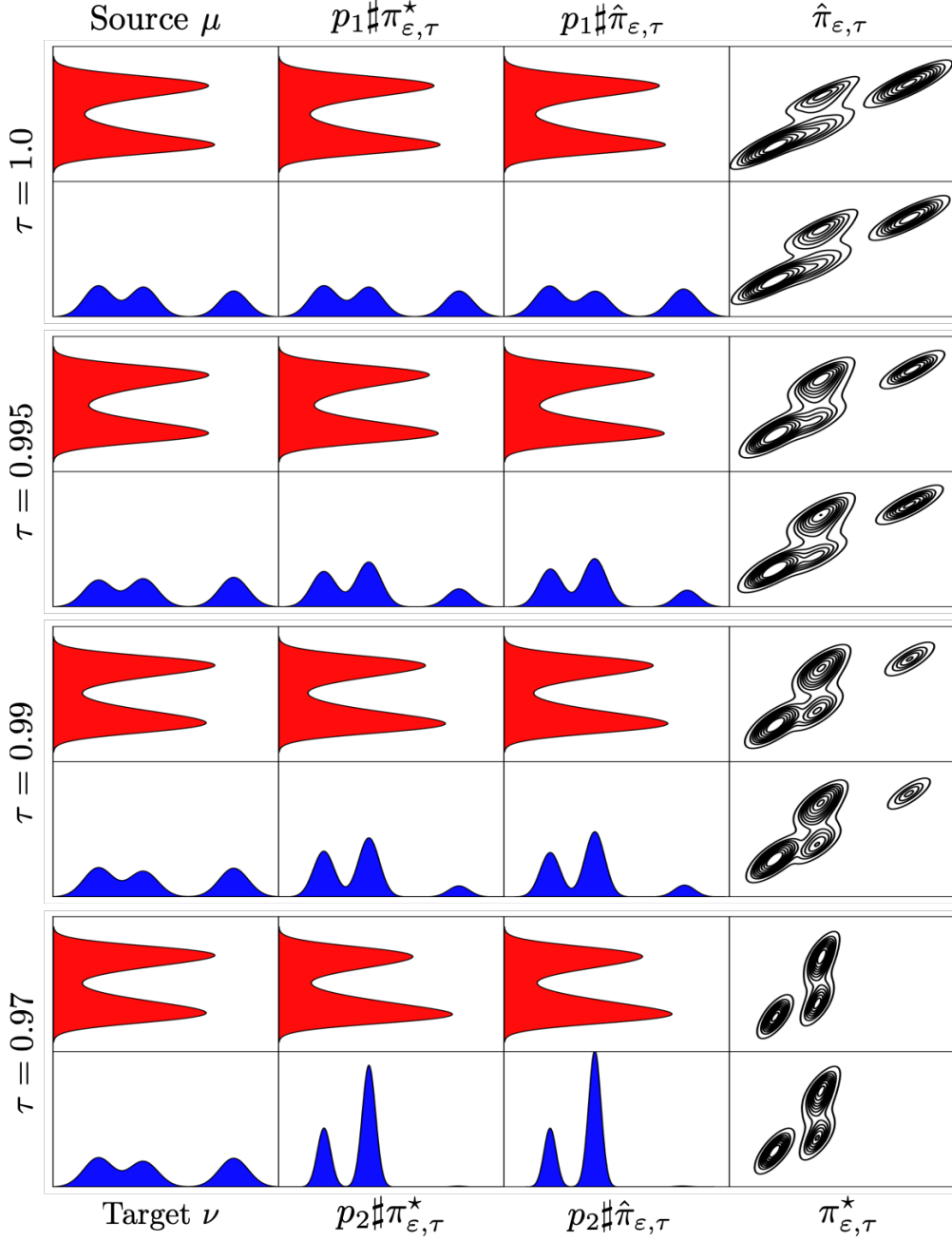


Figure 7: Unbalanced entropic neural optimal transport plan with $\epsilon = 0.05$ and varying unbalanced-ness parameter $\tau = \tau_1 = \tau_2$. Figure 1 shows the results for $\tau = 0.98$.

We benchmark the models with different entropy regularisation parameters ϵ . We also report the conditional mean across 30 samples of the pushforward of GENOT-K (denoted by GENOT-K CM) as it is shown to prove useful in many real-world scenarios (see e.g. section 5.2). Figure 8 shows the superior performance of GENOT-K across all entropy regularisation parameters. While GENOT-K CM performs even better, we would like to highlight that the conditional mean of the pushforward is not expected to follow the target distribution. For Scones (Daniels et al., 2021), we observed that training diverged for $\epsilon \in \{0.1, 0.01, 0.001\}$.

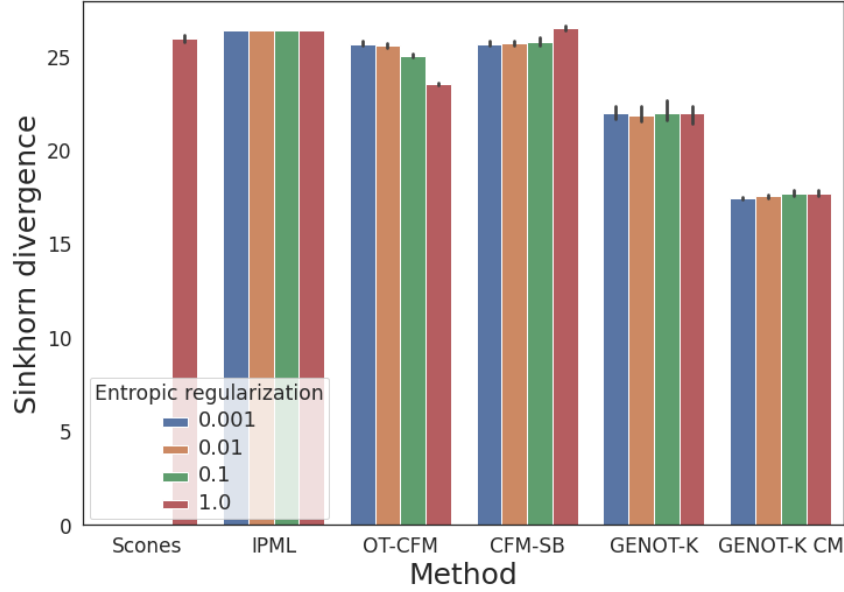


Figure 8: Mean and standard deviation of the Sinkhorn divergence (Feydy et al., 2019b) between test target distribution and pushforward of the test source distribution across three runs on the developing mouse pancreas dataset D.1.

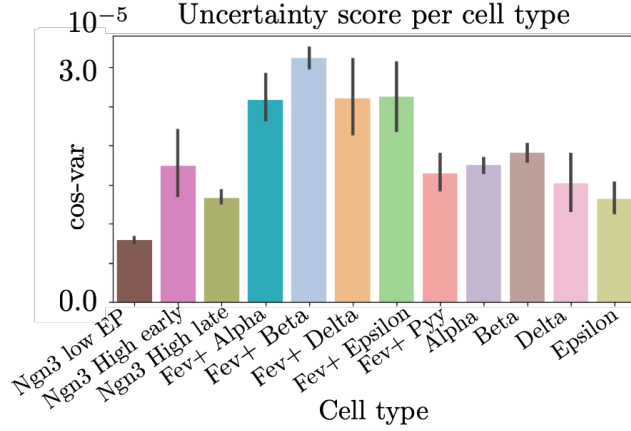


Figure 9: Uncertainty score (appendix C.1) as displayed in figure 2 aggregated to cell type level.

Interpreting the conditional distribution in mouse pancreas development Obtaining samples from the conditional distribution allows for an assessment of the uncertainty of the trajectory of a cell. We use the metric $\text{Var}_{Y \sim \hat{\pi}_\epsilon(\cdot|\mathbf{x})}[\cos\text{-sim}(Y, \mathbb{E}_{Y \sim \hat{\pi}_\epsilon(\cdot|\mathbf{x})}[Y])]$ suggested in Gayoso et al. (2022) for generative RNA velocity models (appendix C.1). Therefore, we use 30 samples from the conditional distribution.

A cell is expected to have an uncertain trajectory when it awaits a lineage decision. In contrast, cells are expected to have a less uncertain trajectory when their descending population is homogeneous or they belong to a terminal cell state, and hence have committed to a certain lineage.

GENOT-K produces meaningful uncertainty assessments as can be seen from figure 2 and figure 9. Indeed, the Ngn3 low EP population has low variance as all of these cells are expected to transition to the Ngn3 high EP population (Bastidas-Ponce et al., 2019; Klein et al., 2023). In the Ngn3 High early population cells undergo a lineage decision towards the Alpha/Beta or the Delta/Epsilon lineage, hence the uncertainty is higher. Afterwards, cells in the Ngn3 High late or in any Fev+ cell

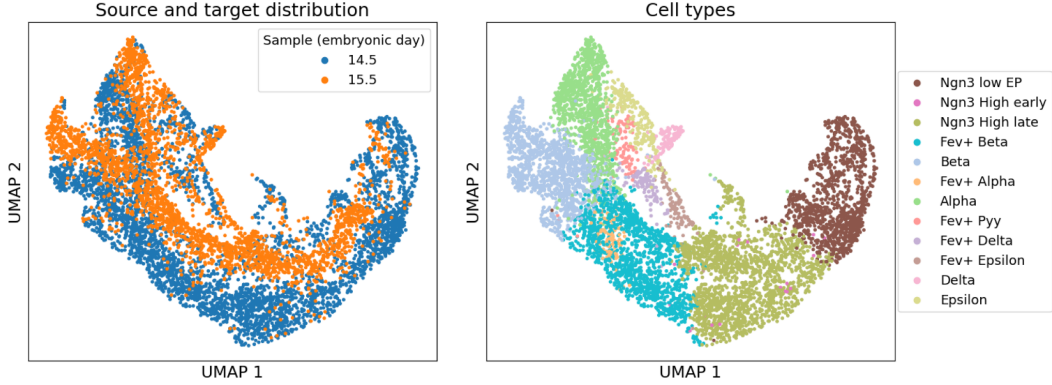


Figure 10: Left: UMAP of the mouse pancreas development dataset colored by sample. We transport samples from embryonic day 14.5 to embryonic day 15.5. Right: UMAP colored by cell type.

$\tau_1 = \tau_2$	1.0	0.999	0.99	0.95	0.90	0.80
CTS	0.660	0.677	0.714	0.786	0.815	0.86
Sinkhorn divergence	19.85	20.15	19.63	21.23	21.78	21.80

Table 1: Cell type transition score (CTS, C.2) for U-GENOT-K and Sinkhorn divergence (Feydy et al., 2019b) between target and predicted target. The results reported are the mean across three runs, see table 2 for the variance.

population await fate decisions, while cells in the mature cell types Alpha, Beta, Delta, and Epsilon have committed to a cell type, and hence their trajectory is less uncertain.

Unbalancedness in mouse pancreas development Due to different rates in proliferation (cell birth) and apoptosis (cell death), as well as sampling biases (e.g. due to cell sorting, also referred to as Fluorescence-activated cell sorting), the incorporation of unbalancedness is crucial for numerous datasets in single-cell biology.

We demonstrate this necessity on the mouse pancreas development dataset. The dataset captures two major lineages originating from the multipotent cell population (hence we drop multipotent cells). One lineage (A) develops into Acinar cells and comprises, additionally to Acinar cells, their progenitor population of Tip cells. On the other hand, we have the endocrine/ductal lineage (ED), comprising all remaining cell types. We use a random 60/40 split into train and test data, and run each U-GENOT-K three times with different seeds. Table 1 shows that U-GENOT-K is able to compensate for the undesired distributional shift to a large extent. Table 2 reports the corresponding variance across three runs.

Figure 11 and figure 12 visualize the mean and standard error of the learnt left and right rescaling functions, grouped by evaluations on the training and test set. We expect the rescaling functions within one cell type to attain similar values, hence this is a way to validate whether the learnt rescaling function is meaningful also on the test set. Indeed, we can see that the mean and standard deviation of the learnt left and right rescaling functions are very similar for evaluations on the training and the test dataset.

Perturbation modeling with GENOT-K and U-GENOT-K For each drug, we project the single-cell RNA-seq readout of the unperturbed and perturbed cells to a 50-dimensional PCA embedding. Subsequently, we split the data randomly to obtain a train and test set with a ratio of 60%/40%. This preprocessing step holds for both the calibration score experiments and the experiments conducted with U-GENOT-K to assess the influence of unbalancedness to the accuracy score.

The uncertainty score for the calibration study is computed based on 30 samples from the conditional distribution, see appendix C.2.

$\tau_1 = \tau_2$	1.0	0.999	0.99	0.95	0.90	0.80
CTS	4.8×10^{-5}	6.0×10^{-5}	6.5×10^{-4}	1.7×10^{-5}	4.2×10^{-5}	2.5×10^{-5}
S. div.	2.9×10^{-2}	5.1×10^{-2}	4.8×10^{-1}	1.4×10^{-2}	5.6×10^{-3}	8.8×10^{-2}

Table 2: Variance of cell type transition score (CTS) and Sinkhorn divergence (S. div.) between target and predicted target of U-GENOT-K across three runs. Means are reported in table 1.

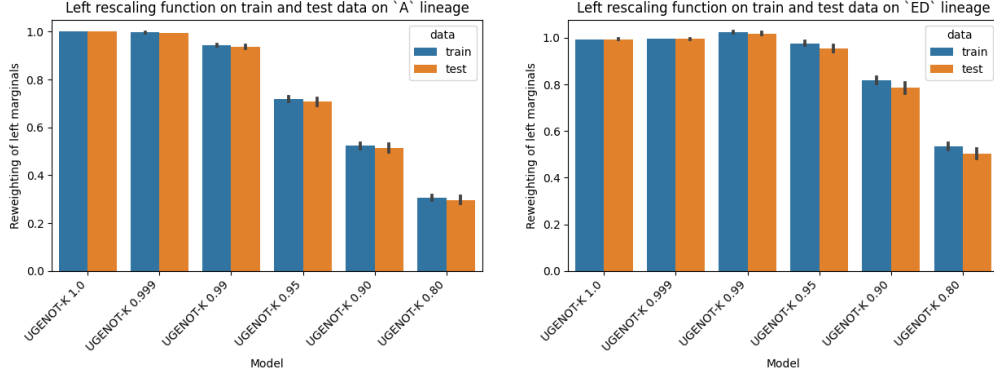


Figure 11: Mean and variance of the predictions of the left rescaling functions on the train and test dataset for different parameters $\tau = \tau_1 = \tau_2$ (denoted as U-GENOT-K τ) across three runs on the full pancreas development dataset. On the left, results are reported for the A lineage, on the right for the ED lineage.

In figure 13 and figure 14, we visualize the influence of unbalancedness for perturbation modeling with Dacinostat and Tanespimycin, respectively. These experiments were conducted on the full dataset for visualization reasons. While the fitting property seems to be little affected by incorporating unbalancedness (top rows), the cell type clusters are better separated for U-GENOT-K transport plans than for GENOT-K transport plans.

E.3 GENOT-GW & GENOT-FGW

GENOT-GW on toy data Here, we explicitly visualize the dependence of the conditional distribution on the entropy regularization parameter ε .

Modality translation with GENOT-GW For all experiments, we perform a random 60-40 split for training and test data. All results are reported on the test dataset. The cost matrices of all models were scaled by its mean and the entropy regularization parameter ε was set to 0.001. Moreover, the models were trained for 5,000 iterations.

Modality translation with GENOT-FGW For all experiments, we perform a random 60-40 split for training and test data. All results are reported on the test dataset. The cost matrices of all models were scaled by its mean and the entropy regularization parameter ε was set to 0.001. Moreover, the models were trained for 20,000 iterations.

Figure 16 reports results of the GENOT-FGW model with interpolation parameter $\alpha = 0.7$. While the Sinkhorn divergences are not comparable with results of the GENOT-GW model due to the respective target distributions living in different spaces, we can compare GENOT-GW with GENOT-FGW with the FOSCTTM score. Figure 16 shows that GENOT-FGW strikingly outperforms GENOT-GW, hence the incorporation of the fused term is crucial for a good performance. At the same time, it is important to mention that the GW terms add valuable information to the problem setting, which can be derived from the results for GENOT-FGW with $\alpha = 0.3$ presented in figure 16. Here, the higher influence of the fused term causes the model to perform overall worse. Interestingly, the geodesic cost approximation performs significantly worse than the squared Euclidean cost with respect to the FOSCTTM score. We note that the construction of the geodesic cost involves multiple hyperparameters, which we did not optimize for. Yet, the fitting term, measured with the

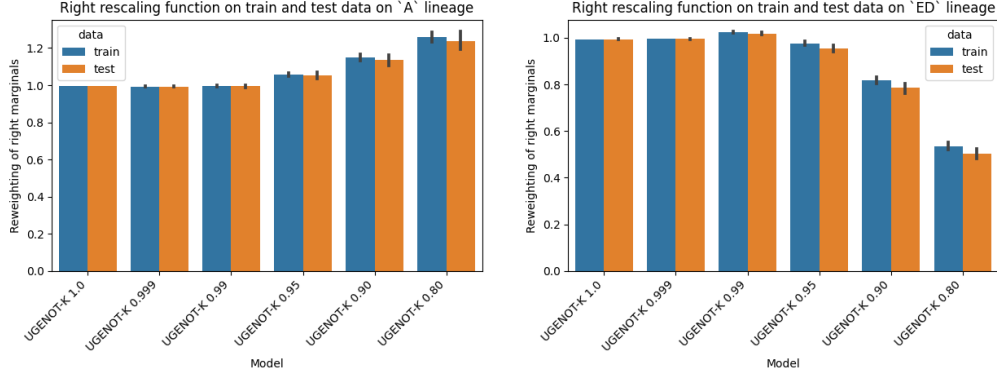


Figure 12: Mean and variance of the predictions of the right rescaling functions on the train and test dataset for different parameters $\tau = \tau_1 = \tau_2$ (denoted as U-GENOT-K τ) across three runs on the full pancreas development dataset. On the left, results are reported for the A lineage, on the right for the ED lineage.

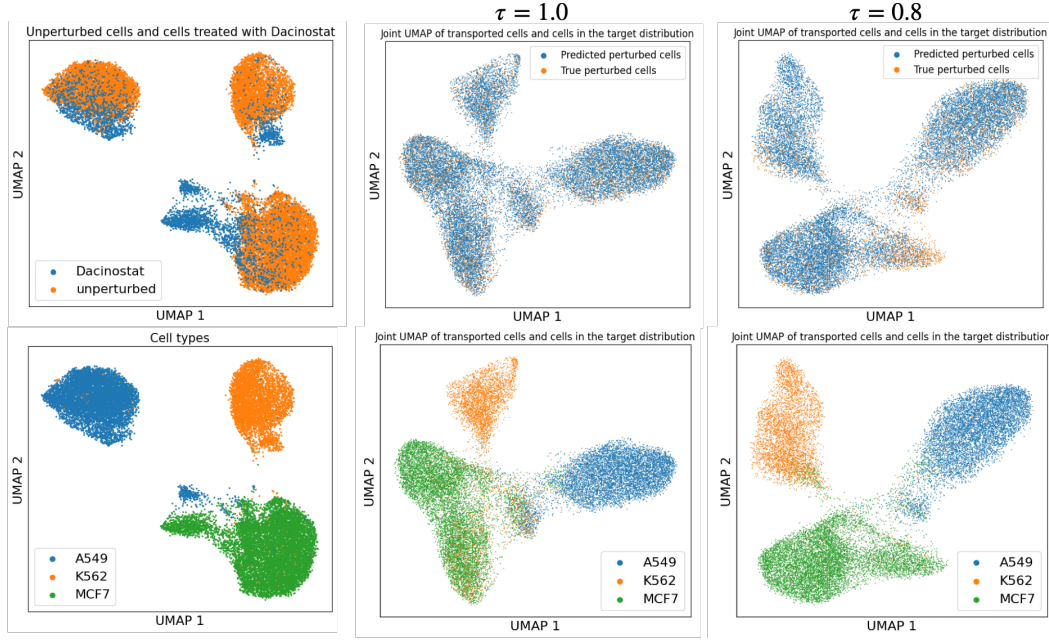


Figure 13: Visual assessment of the influence of unbalancedness in modeling cellular predictions to the cancer drug Dacinostat. In the left column, the source and target distribution are jointly plotted with cells colored by whether they belong to the source (unperturbed) or the target (perturbed) distribution (top), and which cell type they belong to (bottom). In the center column, we plot a UMAP embedding of target and predicted target distribution. The top plot colors cells according to whether a cell belongs to the target distribution or the predicted target distribution. The bottom plot is colored by cell type. The cell type of the predicted target distribution is the cell type of the pre-image of the predicted cell. The right column visualizes the same results, but this time obtained from U-GENOT-K with unbalancedness parameters $\tau = \tau_1 = \tau_2 = 0.8$.

Sinkhorn divergence, does not suffer significantly from the performance loss with respect to the FOSCTTM score.

Moreover, we can visualize the optimality and fitting term in a UMAP embedding (McInnes et al., 2018). To demonstrate the robustness of our model, we train a GENOT-FGW model with $\varepsilon = 0.01$, $\alpha = 0.5$ and the Euclidean distance on 60% of the dataset (38 dimensions for the ATAC LSI embedding, 50 dimensions for the RNA PCA embedding, and 28 dimensions for the VAE

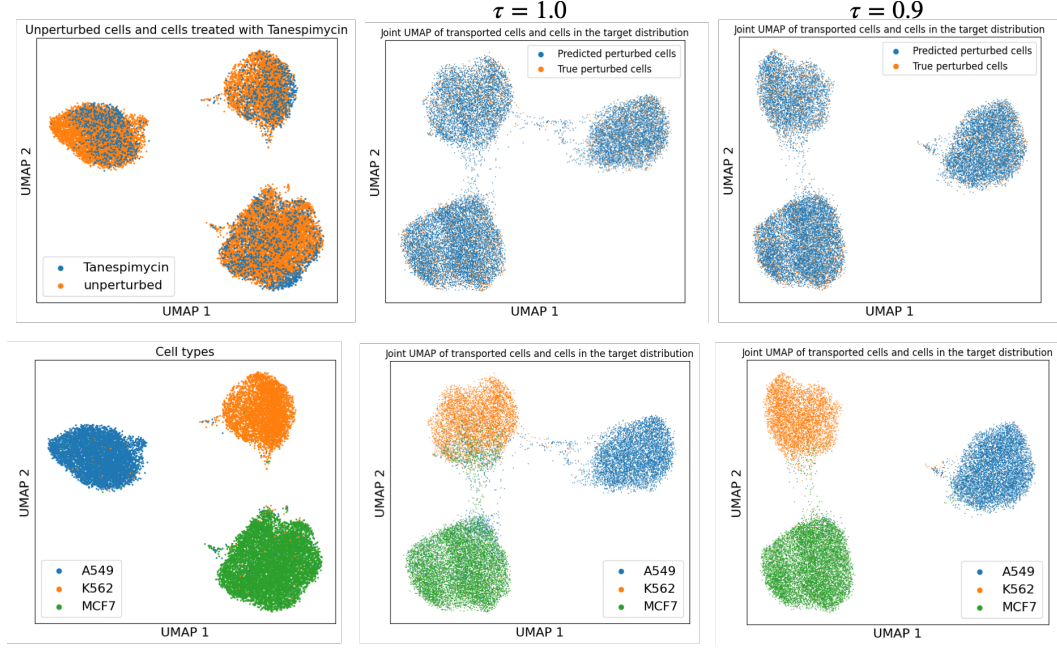


Figure 14: Visual assessment of the influence of unbalancedness in modeling cellular predictions to the cancer drug Tanespimycin. In the left column, the source and target distribution are jointly plotted with cells colored by whether they belong to the source (unperturbed) or the target (perturbed) distribution (top), and which cell type they belong to (bottom). In the center column, we plot a UMAP embedding of target and predicted target distribution. The top plot colors cells according to whether a cell belongs to the target distribution or the predicted target distribution. The bottom plot is colored by cell type. The cell type of the predicted target distribution is the cell type of the pre-image of the predicted cell. The right column visualizes the same results, but this time obtained from U-GENOT-K with unbalancedness parameters $\tau = \tau_1 = \tau_2 = 0.9$.

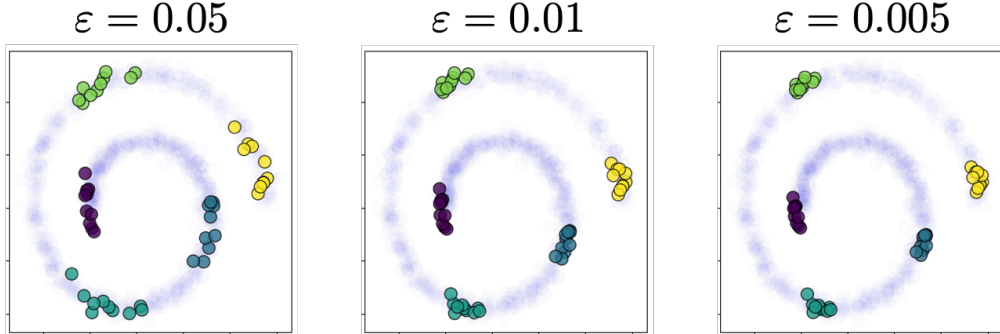


Figure 15: Conditional distribution $\hat{\pi}_\epsilon(\cdot|\mathbf{x})$ for GENOT-GW models trained with different entropy regularization parameter ϵ . The setup is the same as in figure 4, in effect we transport a three-dimensional Swiss roll to a two-dimensional spiral, which is colored in blue (with high transparency). The source distribution as well as the data points which are conditioned on are visualized in figure 4.

embedding in the fused term) and evaluate the learnt transport plan visually. Figure 5 shows the joint UMAP embedding of predicted target and target, the full legend of cell types can be found in figure 18. Qualitatively, a good mix between data points of the predicted target and the target distribution suggests a good fitting term. Optimality of the mapping can be visually assessed by considering to what extent cell types are mixed (low optimality) or separated from other cluster (high optimality). Similarly, figure 19 and figure 20 show the results based on a UMAP embedding created on the fused space (space corresponding to the fused term) only and on a UMAP embedding

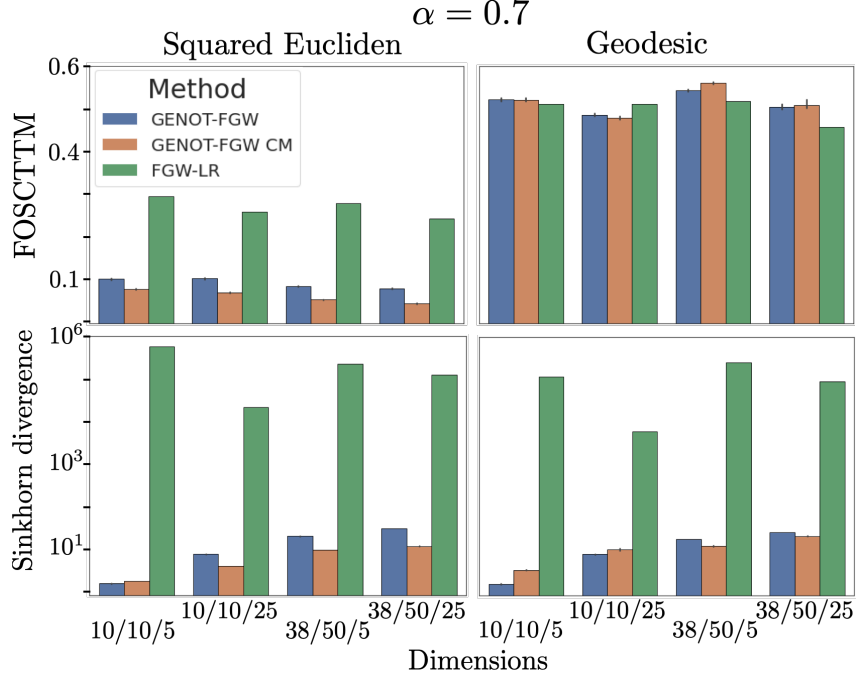


Figure 16: Mean and standard deviation (across three runs) of the FOSCTTM score (top) and the Sinkhorn divergence (bottom) of GENOT-FGW and discrete FGW with linear regression for out-of-sample estimation. Experiments are categorized by the numbers $d_1/d_2/d_3$, where d_1 is the dimension of the space corresponding to the GW of the source distribution, d_2 is the dimension of the space corresponding to the GW of the target distribution, and d_3 is the dimension of the shared space. Results are reported for the interpolation parameter $\alpha = 0.7$. The best performing configuration is GENOT-FGW CM on the embeddings of dimension (38/50/25) with a mean FOSCTTM score of 0.048.

created from the GW space (term corresponding to the GW target term) only, respectively. Note that these UMAP embeddings were created based on a subspace of the space the FGW problem lives on, in particular we do *not* train a GENOT-K or GENOT-GW model. We can see that the target distribution is well matched in both of these spaces separately.

We observed that taking the conditional mean improves results on the FOSCTTM score, but can impair the fitting property. Indeed, the mixing rate between data points belonging to the target and data points belonging to the predicted target seems to be slightly worse when considered in the joint embedding as well as when considering only the fused space and only considering the quadratic space (20).

Modality translation with U-GENOT-FGW To simulate a setting where there is not a match for certain cells in the gene expression dataset, we choose to drop the cells labelled as Proerythroblasts, Erythroblasts, and Normoblasts as these cells form a lineage, developing into mature Reticulocytes (not present in the dataset). Thus, they are similar in their cellular profile while being clearly distinguishable from the remaining cells.

While we keep the right marginals constant, as we have a true match for each cell in the target distribution, we introduce unbalancedness in the source marginals. It is important to note that the influence of the unbalancedness parameters are affected by the number of samples, as well as the entropy regularization parameter ϵ . To demonstrate the robustness of GENOT-FGW with respect to hyperparameters, we still choose $\alpha = 0.7$, but this time set $\epsilon = 5 \cdot 10^{-3}$. We use 50-dimensional PCA-space for the Gromov term in the RNA space, 38-dimensional LSI-space for the Gromov term in the ATAC space, and a 30-dimensional VAE-embedding for the shared space.

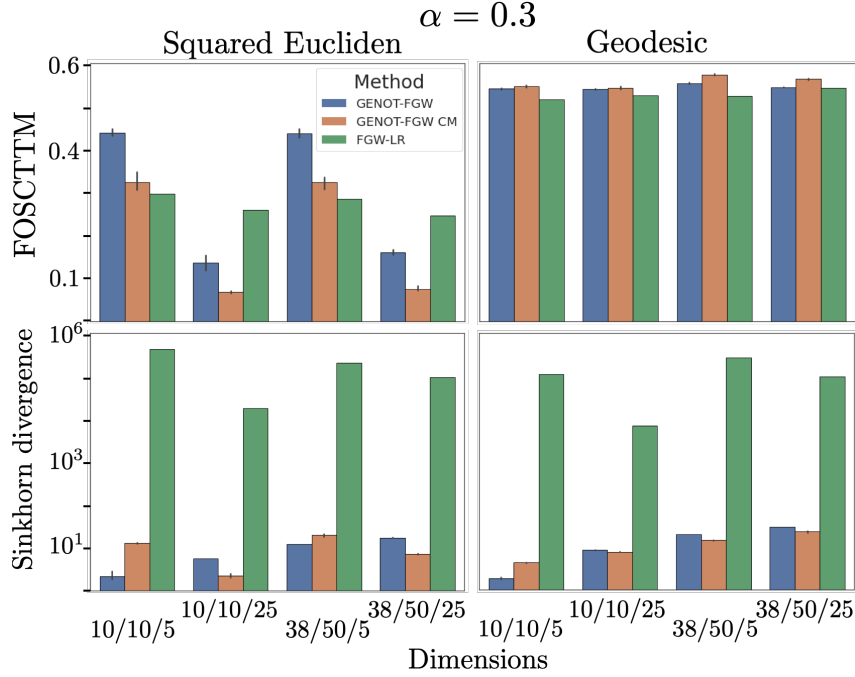


Figure 17: Mean and standard deviation (across three runs) of the FOSCTTM score (top) and the Sinkhorn divergence (bottom) of GENOT-FGW and discrete FGW with linear regression for out-of-sample estimation. Experiments are categorized by the numbers $d_1/d_2/d_3$, where d_1 is the dimension of the space corresponding to the GW of the source distribution, d_2 is the dimension of the space corresponding to the GW of the target distribution, and d_3 is the dimension of the shared space. Results are reported for the interpolation parameter $\alpha = 0.3$. The best performing configuration is GENOT-FGW CM on the embeddings of dimension (10/10/25) with a mean FOSCTTM score of 0.068.



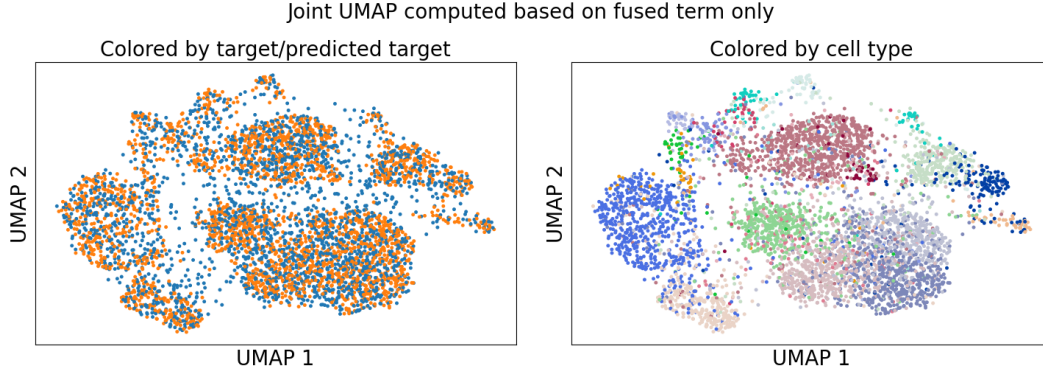
Figure 18: Complete legend of cell types for figures 5, 19, and 20.

The computation of the growth rates for the discrete setting is described in appendix F.2. We perform a random 60-40 split to divide the data into training and test set. The FOSCTTM score only considers those cells which have a true match, i.e. cells in the source distribution belonging to the Normoblast, Erythroblast, and Proerythroblast cell types are not taken into account as their true match was removed from the target distribution.

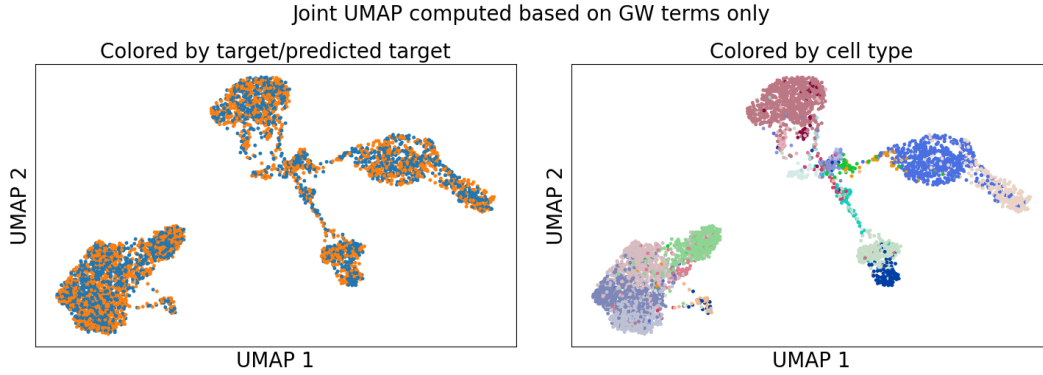
We assess the performance w.r.t. the FOSCTTM score to ensure that the model still learns meaningful results, and consider the average reweighting function $\hat{\eta}$ per cell type (appendix E.3). We consider two values ($\tau_1 = 0.8$ and $\tau_1 = 0.3$) of the left unbalancedness parameter, while $\tau_2 = 1.0$ as for every cell in the target distribution there exists the true match in the source distribution. Table 3 shows that U-GENOT-FGW learns more meaningful reweighting functions than discrete UFGW as the average rescaling function on the left-out cell types is closer to 0, while the mean value of the rescaling function on all remaining cell types ("other") is closer to 1. At the same time, U-GENOT-FGW yields lower FOSCTMM scores and hence learns more optimal couplings.

Table 5 shows the variance across three runs, demonstrating the stability of both the learnt rescaling function as well as the performance with respect to the FOSCTTM score.

Figure 21 and figure 22 show the mean and the standard deviation of the learnt growth rates per cell type. First, it is interesting to see that Normoblasts have the lowest mean of rescaling function evaluations (for both discrete UFGW and U-GENOT-FGW), which is due to them being most mature



a) UMAP embedding created on the space corresponding to the fused term only.



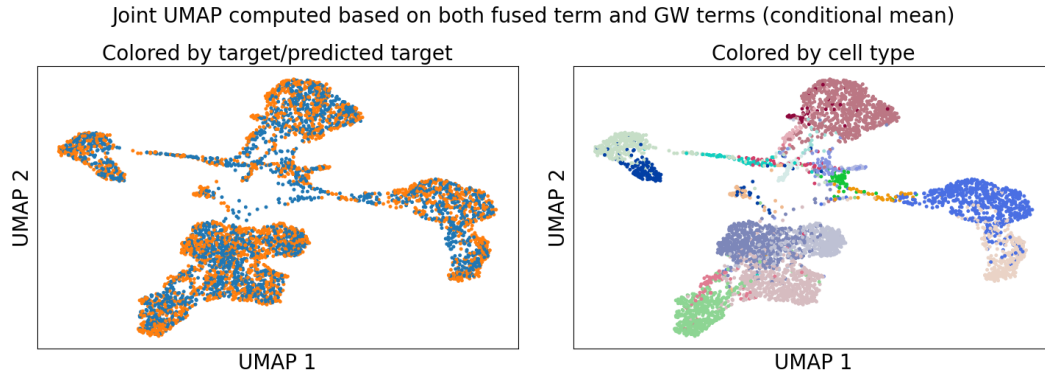
b) UMAP embedding created on the space corresponding to the target GW term only.

Figure 19: UMAP embeddings of predicted target and target. Left panels: Cells are colored based on whether they belong to the target distribution or the predicted target distribution. Right: Cells are colored according to their cell type. For cells which belong to the predicted target distribution, the cell type is defined as the cell type of the preimage. Results are shown on the test data set, corresponding to 40% of the full dataset.

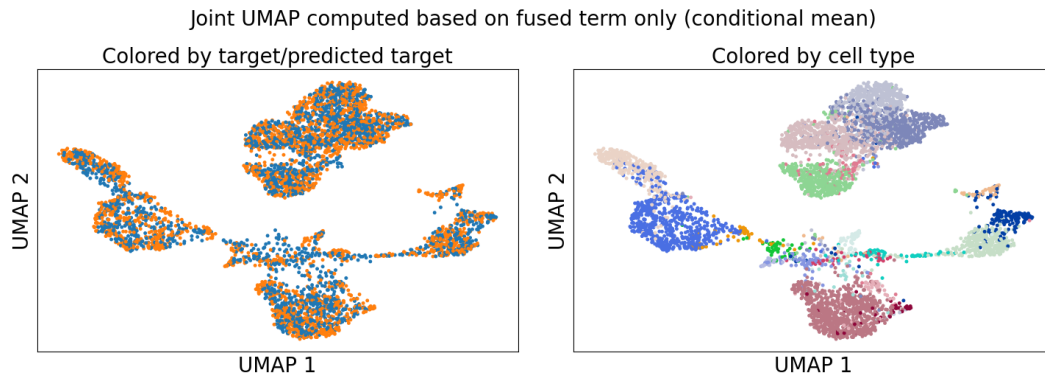
Table 3: Mean value of the rescaling function per cluster for U-GENOT-FGW and discrete unbalanced FGW together with the FOSCTTM scores across three runs. Table 5 reports the variances for the GENOT-GW models.

model (τ_1)	Normoblast	Erythroblast	Proerythroblast	other	FOSCTTM
Discrete UFGW (0.8)	0.788	0.820	0.842	0.945	0.258
U-GENOT-FGW (0.8)	0.622	0.733	0.894	1.077	0.131
Discrete UFGW (0.3)	0.591	0.586	0.734	0.761	0.311
U-GENOT-FGW (0.3)	0.295	0.430	0.554	1.186	0.162

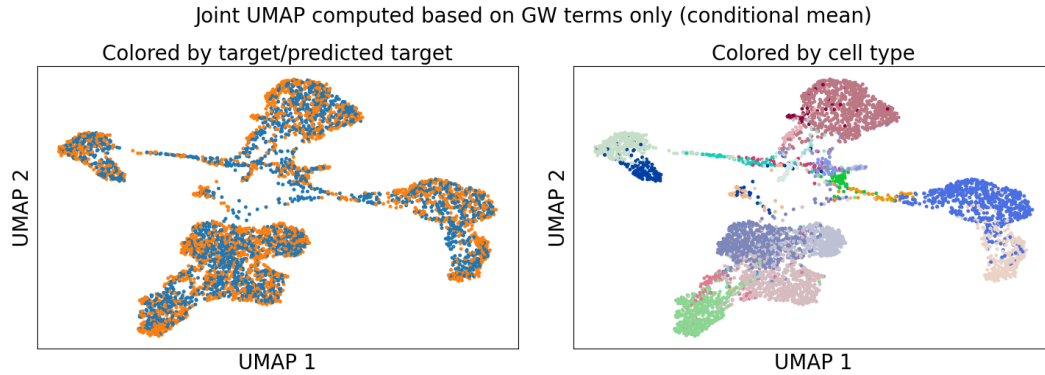
among the left out cell types and hence being furthest away in gene expression space / ATAC space from the common origin of all cells, the HSC cluster. Moreover, it is obvious that the standard deviation of the reweighting function (across cells in one cell type) is much smaller for U-GENOT-FGW than for discrete UFGW. This is desirable as cells within one cell type are very similar in their ATAC profile.



a) UMAP embedding.



b) UMAP embedding created on the space corresponding to the fused term only.



c) UMAP embedding created on the space corresponding to the target GW term only.

Figure 20: UMAP embeddings of predicted target and target for GENOT-FGW CM. Left panels: Cells are colored based on whether they belong to the target distribution or the predicted target distribution. Right: Cells are colored according to their cell type. For cells which belong to the predicted target distribution, the cell type is defined as the cell type of the preimage. Results are shown on the test data set, corresponding to 40% of the full dataset.

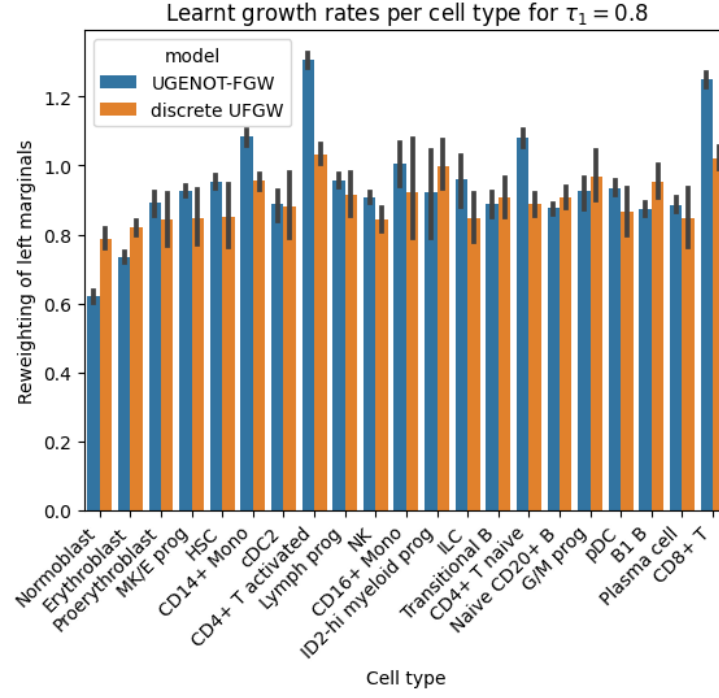


Figure 21: Comparison of learnt growth rates of discrete UFGW and U-GENOT-FGW aggregated to cell type level for unbalancedness parameters $\tau_1 = 0.8$ and $\tau_2 = 1$.

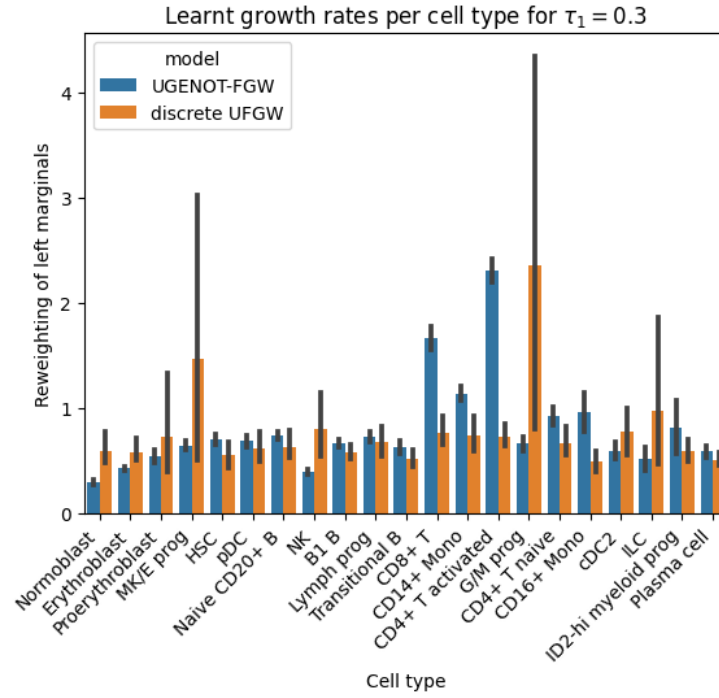


Figure 22: Comparison of learnt growth rates of discrete UFGW and U-GENOT-FGW aggregated to cell type level for unbalancedness parameters $\tau_1 = 0.3$ and $\tau_2 = 1$.

Table 4: Comparison of reweighting functions learnt by U-GENOT-FGW and discrete unbalanced FGW

model (τ_1)	Normoblast	Erythroblast	Proerythroblast	other	FOSCTTM
U-GENOT-FGW (0.8)	$3 \cdot 10^{-6}$	$2 \cdot 10^{-5}$	$1 \cdot 10^{-4}$	$5 \cdot 10^{-5}$	$3 \cdot 10^{-5}$
U-GENOT-FGW (0.3)	$2 \cdot 10^{-6}$	$9 \cdot 10^{-6}$	$5 \cdot 10^{-4}$	$8 \cdot 10^{-4}$	$9 \cdot 10^{-5}$

Table 5: Variance of the mean of the learnt rescaling function per cell type for U-GENOT-FGW across three different seeds.

F COMPETING METHODS

In the following, we discuss the setup of the competing methods. In particular, we discuss the setup for the benchmark on the pancreas dataset in section F.1 and discuss linear regression-based out of sample estimation for discrete Gromov in section F.2.

F.1 ENTROPIC NEURAL OT METHODS

As we choose the same architecture and hyperparameters for the GENOT-models as described in appendix G across experiments and problem settings, we do *not* optimize the hyperparameters of competing methods. In the following, we outline the code based on which we run the benchmarks.

Daniels et al. (2021) We use the configuration provided in <https://github.com/mdnls/scones-synthetic> for the Gaussian data.

Tong et al. (2023b) We use the configuration of the notebook for the single-cell experiments in https://github.com/atong01/conditional-flow-matching/blob/main/examples/notebooks/single-cell_example.ipynb.

Tong et al. (2023a) We use the configuration of the notebook for the single-cell experiments in https://github.com/atong01/conditional-flow-matching/blob/main/examples/notebooks/single-cell_example.ipynb.

Vargas et al. (2021) We follow the code provided at <https://github.com/AforAnonyMeta/IPML-2548>, specifically the configuration for the single-cell experiments (https://github.com/AforAnonyMeta/IPML-2548/blob/main/script/EB_Dataset.py). We set the *gp_prior* to *None* as the model runs out of memory otherwise (for the given datasets).

F.2 REGRESSION FOR OUT-OF-SAMPLE DATA POINTS

Out-of-sample prediction for GW has been considered in Alvarez-Melis & Jaakkola (2018). Yet, their methods rely on an orthogonal projection, which only works if both the sample size and the feature dimensions are the same in both spaces. Hence, we rely on a barycentric projection for in-sample data points. For out-of-sample data points we project a data point onto the training set and apply the barycentric projection to the linear combination of points in the in-sample distribution. Let $\mathbf{X} \in \mathbb{R}^{n \times d}$ be the matrix containing n in-sample data points.

Then, for a data point in the source distribution $\mathbf{x} \in \mathbb{R}^d$, let

$$\hat{\beta}_{\mathbf{x}} = \arg \min_{\beta \in \mathbb{R}^n} \|\hat{\mathbf{x}} - \mathbf{X}^T \beta\|_2^2 \quad (43)$$

where the sum is taken over the n in-sample data points. Moreover, let $p_i = \sum_{j=1}^m \Pi_{ij}$. Then, the barycentric projection of a point in the source distribution is given as

$$\hat{\mathbf{y}} = \sum_{i=1}^n \frac{\hat{\beta}_i}{p_i} \sum_{j=1}^m \Pi_{ij} \mathbf{y}_j \in \mathcal{Y}. \quad (44)$$

Similarly, we can apply this procedure to estimate rescaling factors in the unbalanced setting. To ensure non-negativity of the rescaling function, we perform regression with non-negative weights:

$$\hat{\alpha}_{\mathbf{x}} = \arg \min_{\alpha \in \mathbb{R}_{\geq 0}^n} \|\hat{\mathbf{x}} - \mathbf{X}^T \alpha\|_2^2 \quad (45)$$

To estimate the rescaling function for a data point \hat{x} , the estimated left rescaling function is given as

$$\hat{\eta} = \sum_{i=1}^n \hat{\alpha}_i \eta_i \in \mathbb{R} \quad (46)$$

where $\{\eta_i\}_{i=1}^n$ is the set of reweighting function evaluations of in-sample data points.

G IMPLEMENTATION

The GENOT framework is implemented in JAX Bradbury et al. (2018). Discrete OT solvers are provided by OTT-JAX Cuturi et al. (2022).

G.1 PARAMETERIZATION OF THE VECTOR FIELD

The vector field is parameterized with a feed-forward neural network which takes as input the time, the condition (i.e. the samples from the source distribution) and the latent noise. Each of these input vectors are independently embedded by one block of layers before the embeddings are concatenated and applied to another block of layers, followed by one output layer. If not stated otherwise, one block of layers consists of 8 layers of width 256 with *silu* activation functions.

G.2 PARAMETERIZATION OF THE RESCALING FUNCTIONS

Rescaling functions are parameterized as feed-forward neural networks with 5 layers of width 128, followed with a final *softplus* activation function to ensure non-negativity.

G.3 TRAINING DETAILS

In the following, we report default values for different parameters of the GENOT models. If not stated otherwise in the corresponding experiments section, these parameters are used:

- number of training iterations: 10,000
- optimizer: AdamW with learning rate $1e - 4$ and weight decay $1e - 10$ (also for learning the rescaling functions)
- entropy regularisation parameter $\varepsilon = 1e - 2$
- by default, we do not scale the cost matrix for the computation of the discrete OT solver
- cost function: squared Euclidean distance (we always use the same cost for all terms, even if it would be possible to choose different costs in separate spaces in the GW and FGW settings)
- batch size: 1024
- number of samples from the conditional distribution: 1

When using the graph distance, we construct a k-nearest neighbor graph with *batch_size*+1 number of edges. For the approximation of the heat kernel, we use the default parameters provided by the implementation in OTT-JAX (Cuturi et al., 2022).